INSTITUT DE FRANCE
Académie des sciences

Comptes Rendus

Géoscience

Sciences de la Planète

Marco Liuzzo, Andrea Di Muro, Andrea Luca Rizzo, Fausto Grassa, Massimo Coltorti and Magali Ader

The composition of gas emissions at Petite Terre (Mayotte, Comoros): inference on magmatic fingerprints

Published online: 15 September 2022

https://doi.org/10.5802/crgeos.148

Part of Special Issue: The Mayotte seismo-volcanic crisis of 2018-2021 in the Comoros archipelago (Mozambique channel)

Guest editors: Jérôme Van der Woerd (Institut Terre Environnement de Strabourg, UMR 7063 CNRS / Université de Strasbourg, 67084 Strasbourg, France), Vincent Famin (Laboratoire Géosciences Réunion, Université de La Réunion - IPGP, 97744 Saint-Denis, France) and Eric Humler (Professeur Université de Nantes, Laboratoire de Planétologie et Géosciences, UMR 6112, Faculté des Sciences et Techniques, Nantes Université, 44322 Nante, France)

Les Comptes Rendus. Géoscience — Sciences de la Planète *sont membres du Centre Mersenne pour l'édition scientifique ouverte*
www.centre-mersenne.org
e-ISSN : 1778-7025

Comptes Rendus
Géoscience — Sciences de la Planète
Published online: 15 September 2022
https://doi.org/10.5802/crgeos.148

The Mayotte seismo-volcanic crisis of 2018-2021 in the Comoros archipelago (Mozambique channel) / *La crise sismo-volcanique de 2018-2021 de Mayotte dans l'archipel des Comores (Canal du Mozambique)*

The composition of gas emissions at Petite Terre (Mayotte, Comoros): inference on magmatic fingerprints

Marco Liuzzo [*, a, b], **Andrea Di Muro** [c, d], **Andrea Luca Rizzo** [a, e], **Fausto Grassa** [a], **Massimo Coltorti** [b] and **Magali Ader** [c]

[a] Istituto Nazionale di Geofisica e Vulcanologia, Sezione di Palermo, Italy

[b] Università di Ferrara, Dipartimento di Fisica e Scienze della Terra, Italy

[c] Université de Paris, Institut de physique du globe de Paris, CNRS, F-75005 Paris, France

[d] Observatoire volcanologique du Piton de la Fournaise, Institut de physique du globe de Paris, F-97418 La Plaine des Cafres, France

[e] Istituto Nazionale di Geofisica e Vulcanologia, Sezione di Milano, Italy

E-mails: marco.liuzzo@ingv.it (M. Liuzzo), dimuro@ipgp.fr (A. Di Muro), andrea.rizzo@ingv.it (A. L. Rizzo), fausto.grassa@ingv.it (F. Grassa), clt@unife.it (M. Coltorti), ader@ipgp.fr (M. Ader)

Abstract. The Comoros archipelago is an active geodynamic region located in the Mozambique Channel between East continental Africa and Madagascar. The archipelago results from intra-plate volcanism, the most recent eruptions having occurred on the youngest island of Grande Comore and on the oldest one of Mayotte. Since 2018, the eastern submarine flank of Mayotte has been the site of one of the largest recent eruptive events on Earth in terms of erupted lava volume. On land, the most recent volcanic activity occurred in Holocene on the eastern side of Mayotte, corresponding to the small Petite Terre Island, where two main and persistent gas seep areas are present (Airport Beach, namely BAS, and Dziani Dzaha intracrateric lake). The large submarine eruption at the feet of Mayotte (50 km offshore; 3.5 km b.s.l.) is associated with deep (mantle level) seismic activity closer to the coast (5–15 km offshore) possibly corresponding to a single and large magmatic plumbing system. Our study aims at characterizing the chemical and isotopic composition of gas seeps on land and assesses their potential link with the magmatic plumbing system feeding the Mayotte volcanic ridge and the recent submarine activity. Data from bubbling gases collected between 2018 and 2021 are discussed and compared with older datasets acquired between 2005 and 2016 from different research teams. The relation between $^3He/^4He$ and $\delta^{13}C\text{-}CO_2$ shows a clear magmatic origin for Mayotte bubbling gases, while the variable proportions and isotopic signature of CH_4 is related to the occurrence of both biogenic and abiogenic sources of methane. Our new dataset points to a time-decreasing influence of the recent

* Corresponding author.

seismo-volcanic activity at Mayotte on the composition of hydrothermal fluids on land, whose equilibrium temperature steadily decreases since 2018. The increased knowledge on the gas-geochemistry at Mayotte makes the results of this work of potential support for volcanic and environmental monitoring programs.

Keywords. Gas-geochemistry, Hydrothermal system, Biogenic vs abiogenic CO_2 & CH_4, Stable and noble gas isotopes, Mayotte, Comoros.

Published online: 15 September 2022

1. Introduction

The Comoro Islands form an archipelago located in the Mozambique Channel between the east coast of Africa and the north-western coast of Madagascar. The formation of a huge submarine volcanic edifice since 2018, about 50 km offshore east of Mayotte, has focused the attention of the volcanological community with an increasing number of geophysical, petrological and geochemical studies [Bachèlery et al., 2019, Berthod et al., 2021a,b, Cesca et al., 2020, Feuillet et al., 2019, Lemoine et al., 2020, Liuzzo et al., 2021, Foix et al., 2021, Aiken et al., 2021].

The archipelago consists of four major volcanic islands from NW to SE: Grande Comore, Moheli, Anjouan, and Mayotte (Figure 1). Among them, Grande Comore hosts the frequently active basaltic shield Karthala volcano, whose last eruption occurred in 2007 [Thivet et al., 2022]. Subaerial Holocene volcanic activity related to alkaline magmas whose composition ranges from basanite to phonolite has been documented on the other islands [Bachèlery and Hémond, 2016, Michon, 2016, Tzevahirtzian et al., 2021, Quidelleur et al., 2022]. Based on a review of the existing morphological, geological and chronological data of The Comoro Islands, Tzevahirtzian et al. [2021] suggest that Mayotte and Moheli are the oldest islands, while Anjouan and Grande Comore are the most recent ones. The Comoro Islands are considered as part of the potentially diffuse Lwandle–Somali sub-plate boundary and possibly related to the SE extension of the East African Rift System [Michon, 2016, Famin et al., 2020, Stamps et al., 2021].

The islands of the Comoros archipelago are located within a particularly complex geodynamic region, whose volcanic and tectonic features are yet to be definitively constrained [Coffin et al., 1986, Gaina et al., 2013, Lemoine et al., 2020, Phethean, 2016]. In this complex frame, only limited information exists on the signatures and sources of fluids and their potential link with the recent volcano-tectonic activity [Liuzzo et al., 2021].

At Mayotte, volcanic products becomes increasingly older moving from the eastern side (Petite Terre island), to the western main island (Grande Terre) [Nehlig et al., 2013]. The large-volume and long-lasting submarine eruption of Mayotte, the largest submarine event ever detected by monitoring networks [Berthod et al., 2021a,b, Cesca et al., 2020, Famin et al., 2020, Lemoine et al., 2020, Feuillet et al., 2021] is likely to have had a large scale impact on fluid emissions and compositions. Since 2018, about 6.5 km^3 of evolved basanite lava have been emitted on the 3.5 km deep seafloor, 50 km east southeast from Mayotte from a deep source located in the upper lithospheric mantle [Bachèlery et al., 2019, Berthod et al., 2021a,b, Lemoine et al., 2020, Feuillet et al., 2021]. The new volcano grows on a N120° oriented volcanic ridge, which runs along the eastern submarine flank of Mayotte and its western subaerial tip is the small island of Petite Terre [Tzevahirtzian et al., 2021]. Since the beginning of the crisis, the region has experienced thousands of earthquakes with $M > 3.5$, related to deep (25–55 km depth) sources and distributed in two main swarms: a distal one (25 km away from Petite Terre) and a proximal one (5–15 km from Petite Terre) [Foix et al., 2021]. The important subsidence recorded by GNSS and Insar at Mayotte has been related to the drainage of a large magma reservoir located at mantle level [Lemoine et al., 2020], possibly located at a relatively small distance (13–22 km) from Petite Terre [Foix et al., 2021]. Mayotte Island is thus an ideal playground to study the possible influence of large mafic eruptions on the fluid emissions at regional scale.

On Petite Terre, recent volcanic activity has resulted in a set of Holocene basaltic scoria cones and phonolitic maars formed upon the existing coral reef [Zinke et al., 2001, Nehlig et al., 2013], as well as two main areas of low-temperature CO_2-rich gas seeps (Figure 1). A first bubbling area occurs in the NE part of Petite Terre (Figure 1c) inside the crater lake hosted by the Dziani Dzaha phonolitic maar. Dziani Dzaha

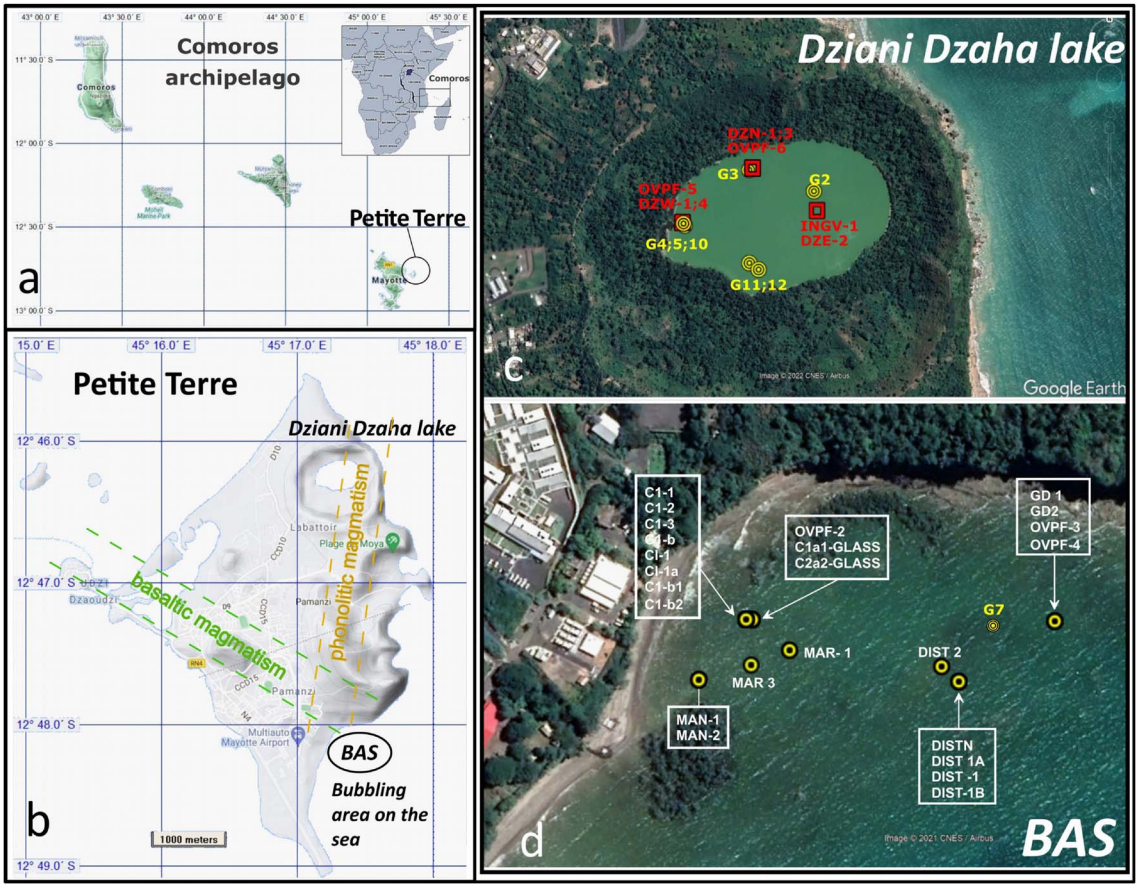

Figure 1. Map of the Comoros archipelago located in the northern part of the Mozambique Channel between Africa and Madagascar. In (b) the map of the Petite Terre Island on the east coast of Mayotte hosting the two main areas of gas seeps on land and where all samples discussed in this paper have been collected. In (c) and (d) the Dziani Dzaha Lake and bubbling area Airport tidal flat (BAS area) respectively. Labeled spots correspond to the location of sampled bubbling pools.

Lake is a meromictic lake with a maximum depth ranging between 4.5 m to around 18 m in a sub-central narrow depression and the bubbling emissions are heterogeneously distributed along the lake margins and in the central area, therefore upwelling through a variable water column in term of depth. Several CO_2-rich and high-flux bubbling areas occur along the lake margins and a main CH_4-rich spot made of myriads of small bubbles occurs close to the deepest part of the lake [Milesi et al., 2020]. A second bubbling area—first described in 1998 on the eastern tidal flat of Petite Terre—is located close to the locality named "Airport beach" [Figure 1d, BAS site; Traineau et al., 2006, Sanjuan et al., 2008]. There, tens of bubbling spots with variable flux occur at the southern base of the large "Vigie" phonolitic maar, on a muddy flat area exposed to significant tide and extended for about 250 × 300 m from the beach.

In this work, we focus on these two bubbling emission zones on Petite Terre Island, with the aim of characterizing their geochemical and isotopic signatures, by constraining their sources and assessing the potential influence of the still ongoing submarine volcano-tectonic activity.

2. Materials and methods

Since the beginning of the seismo-volcanic crisis in May 2018 at Mayotte [Feuillet et al., 2021], five campaigns including geochemical surveys were

carried out, i.e. in December 2018, April 2019, September 2019, November 2020 and September 2021 (Tables 1a–1e).

Bubbling gases were sampled using a steel funnel (on the tidal flat) or a floating plastic funnel (on the Dziani Dzaha Lake) connected to a three-way valve equipped with a syringe and a tube connected to two-stopcock glass bottles of 250 mL (for general chemistry and C–H isotopic analysis), two-stopcock steel bottles of 100 mL (noble gases elemental and isotopic analysis), and pre-weighed evacuated bottles containing 4N NaOH absorbing alkaline solution (for noble gases elemental and isotopic analysis) following the method of Giggenbach and Goguel [1989].

All gas samples were analyzed at the laboratories of the INGV (Istituto Nazionale di Geofisica e Vulcanologia; Section of Palermo), for their chemistry and for the isotopic compositions of noble gases (He, Ne, and Ar), C of CO_2, and C and H of CH_4, except for the last campaign of September 2021 for which only the chemistry of the gases was analyzed and discussed in this work. Results are reported in Tables 1a–1e.

The gas chemistry was determined using a gas chromatograph (GC, Agilent 7890 equipped with PPU and MS5A columns) associated with a MicroGC module (equipped with a PPU column) and a double detector (TCD and FID) using argon as carrier gas. The analytical errors were <3%.

The C-isotope composition of CO_2 (expressed as $\delta^{13}C‰$ versus V-PDB) was determined using a continuous-flow isotope-ratio mass spectrometer (Thermo Delta Plus XP, Finnigan), connected to a gas chromatograph (Trace GC) and an interface (Thermo GC/C III, Finnigan). The gas chromatograph and its column (length = 30 m and i.d. = 0.32 mm; Poraplot-Q) were operated at a constant temperature of 50 °C using He as carrier gas. The analytical errors were <0.1‰. The same instrument was used for measuring the $\delta^{13}C$ and $\delta^{2}H$ of CH_4, where a combustion interface (Thermo GC III, Finnigan) was used to produce CO_2 from CH_4 and a gas-chromatograph/thermal-conversion interface provided online high-temperature conversion of CH_4 into H_2. The SDs for the $\delta^{13}C$ and $\delta^{2}H$ measurements of CH_4 were <0.2 and <2.5‰, respectively.

The He, Ne and Ar isotopic compositions were measured at the noble-gas laboratory of the INGV-Palermo. The ^{3}He and ^{4}He were measured into a split flight tube mass spectrometer (GVI-Helix SFT), after purification of the sample from the major gaseous species using four GP-50 Zr–Al getters and separation from the other noble gases with a trap filled with active charcoal and submerged in liquid nitrogen (for adsorbing argon), and a cryogenic trap equipped with a cold head (Janis Research) cooled down at a temperature of 10 K by a helium compressor and temperature controller that allows regulating the T in order to adsorb and release helium and neon. The ^{20}Ne was measured by admitting Ne into a multicollector mass spectrometer (Thermo-Helix MC plus), after purification procedure into a stainless steel ultra-high vacuum line distinct from that used for He and Ar. The $^{3}He/^{4}He$ ratio is expressed as R and normalized to R_a, the atmospheric helium isotope ratio equal to 1.39×10^{-6}. Analytical uncertainty (1σ) varied between 0.5 and 1.1%. Further details on the purification and analytical procedures can be found in Rizzo et al. [2019].

In the following section, we discuss the $^{3}He/^{4}He$ ratio corrected for atmospheric contamination (expressed as R_c/R_a) using the measured $^{4}He/^{20}Ne$ ratio (see Appendix A, Equation (A1) for the mathematical treatment). The Ar elemental and isotopic compositions (^{36}Ar, ^{38}Ar, and ^{40}Ar) were quantified in a multicollector mass spectrometer (Helix MC-GVI). The analytical uncertainty (1σ) for single $^{40}Ar/^{36}Ar$ measurements was <0.1%. The ^{40}Ar was corrected for air contamination ($^{40}Ar^{*}$) in samples showing $^{40}Ar/^{36}Ar > 315$ to exclude the most air contaminated samples, whose ^{40}Ar correction could lead to over corrections (i.e., underestimation of $^{40}Ar^{*}$), assuming that the detected ^{36}Ar was derived from atmosphere (Appendix A, Equation (A2)). The analytical uncertainty (1σ) of $^{4}He/^{40}Ar^{*}$ and $^{4}He/^{20}Ne$ ratios is below 0.8 and 0.7%, respectively. Typical blanks for He, Ne, and Ar were $<10^{-11}$, $<10^{-12}$, and $<10^{-10}$ cc STP, respectively, and are at least two orders of magnitude lower than the signals obtained during sample measurements. Further details on sample purification and analyses are described by Rizzo et al. [2019] and Boudoire et al. [2020].

3. Results

Tables 1a–1e show the analyses of all samplings, also including the analyses of some data that, by their nature, were affected by air contamination during

Table 1a. Chemical composition of major and minor gaseous components and isotopic values of CO_2 and CH_4 from bubbling area at Petite Terre (surveys 2018–2020)

Sampling date	Sample	Lat	Long	Site	Major (Raw)							$\delta^{13}C$ (‰)		δD (‰)
					CO_2 (vol%)	CO (ppmv)	CH_4 (ppmv)	N_2 (vol%)	O_2 (vol%)	H_2 (ppmv)	He (ppmv)	CO_2	CH_4	CH_4
08/11/2020	OVPF-1	−12.8002	45.2874	BAS	97.5	0.8	3859.0	0.7	0.1	18.0	26.0	−4.4	−18.9	
08/11/2020	C1a1-glass	−12.8002	45.2874	BAS	51.8	1.3	2046.0	36.9	10.0	3.8	13.0			
08/11/2020	OVPF-2	−12.8002	45.2874	BAS	97.2	0.6	3787.0	0.6	0.2	17.0	23.0	−4.3	−19.1	
08/11/2020	C2a2-glass	−12.8002	45.2874	BAS	0.9	1.4	16.0	76.4	20.4	4.0	4.7			
08/11/2020	OVPF-3	−12.8002	45.2895	BAS	97.7	36.0	5291.0	0.5	0.0	82.0	20.0	−4.2	−19.2	−135.0
08/11/2020	GD-1	−12.8002	45.2895	BAS	49.5	1.5	2495.0	38.7	10.4	3.7	9.0			
08/11/2020	OVPF-4	−12.8002	45.2895	BAS	97.7	bdl	5145.0	0.6	0.1	218.0	19.0	−4.2	−19.9	−138.0
08/11/2020	GD-2	−12.8002	45.2895	BAS	73.6	bdl	3600.0	20.7	5.4	2.4	13.0			
10/11/2020	C1-b1	−12.8002	45.28736	BAS	97.1	bdl	3958.0	0.7	0.1	28.0	28.0	−4.6	−19.1	−125.0
10/11/2020	C1-b2	−12.8002	45.28736	BAS	98.8	bdl	3907.0	0.4	0.1	bdl	26.0			
08/09/2019	Dist N	−12.8006	45.28883	BAS	97.1		2854.0	0.3	0.0		25.0	−4.1	−21.6	
08/09/2019	Dist N	−12.8006	45.28883	BAS	98.5		2982.0	0.4	0.0	112.0	26.0	−4.0	−21.8	
08/09/2019	C1-2	−12.8002	45.28736	BAS	98.7		2444.0	0.3	0.1		29.0	−4.7	−21.0	
08/09/2019	C1-2	−12.8002	45.28736	BAS	97.3		2384.0	0.5	0.1	16.0	28.0	−4.7	−19.2	
13/09/2019	Dist 2	−12.8005	45.28871	BAS	98.3	1.2	2914.0	0.3	0.1		27.0	−3.8	−22.0	
08/09/2019	DIST-1	−12.8006	45.28883	BAS		18.0	390000.0	43.1	15.8	8.0	3558.0		−22.1	−137.8
08/09/2019	C1-2	−12.8002	45.28736	BAS		4.1	455400.0	48.0	3.0	11.0	5528.0		−19.6	−118.1
06/04/2019	Dist 1-A	−12.8006	45.28883	BAS	97.1	1.2	2442.0	0.5	0.2	<1	21.0	−3.7	−24.4	
06/04/2019	Dist 1-B	−12.8006	45.28883	BAS	95.8	2.4	2426.0	1.7	0.5	<1	20.0	−3.6		
06/04/2019	Dist 2	−12.8005	45.28871	BAS	97.3	2.1	2406.0	0.3	0.1	<1	19.0	−3.5	−21.4	
06/04/2019	C1-1	−12.8002	45.28736	BAS	97.0	2.1	2088.0	0.8	0.2	<1	23.0	−4.2	−19.0	
06/04/2019	C1-3	−12.8002	45.28736	BAS	97.0	5.0	2036.0	0.9	0.2	<1	23.0	−4.3	−19.0	
06/04/2019	MAR 3	−12.8005	45.28740	BAS	96.5	10.0	2725.0	1.6	0.4	<1	27.0	−4.2	−21.0	
16/12/2018	MAR-1	−12.8004	45.28766	BAS	63.3	1.6	1209.0	27.8	7.5	2.2	7.0			
16/12/2018	MAR-1	−12.8004	45.28766	BAS								−4.8		
16/12/2018	CI-1a	−12.8002	45.28736	BAS	28.7	2.1	416.0	55.0	15.0	<1	bdl	−4.5	−18.7	
16/12/2018	C1-b	−12.8002	45.28736	BAS	97.9	1.7	2130.0	0.7	0.1	318.0	23.0	−4.5		
16/12/2018	CI-1	−12.8002	45.28736	BAS								−4.9		
16/12/2018	MAN-1	−12.8006	45.28705	BAS	95.5	0.7	4587.0	2.5	0.2	<1	107.0	−5.1	−12.4	
16/12/2018	MAN-1	−12.8006	45.28705	BAS								−5.6		
16/12/2018	MAN-2	−12.8006	45.28705	BAS	83.5	8.0	4621.0	12.0	2.7	<1	110.0	−5.0	−11.7	
16/12/2018	MAN-2	−12.8006	45.28705	BAS								−5.7		
09/11/2020	OVPF-5	−12.7708	45.2858	DZIANI	93.2	bdl	4707.0	3.3	1.2	11.0	41.0	−3.1	−27.1	−145
09/11/2020	DZW-1	−12.7708	45.2858	DZIANI	97.3	0.3	4825.0	1.1	0.9	8.0	38.0	−2.6	−26.9	−161
09/11/2020	DZW-4	−12.7708	45.2858	DZIANI	bdl	8.0	258400.0	40.8	31.0	392.0	2322.0		−26.9	−148
09/11/2020	DZW4-dupl	−12.7708	45.2858	DZIANI										
09/11/2020	OVPF-6	−12.7694	45.2877	DZIANI	85.8	bdl	37800.0	8.5	0.3	12.0	1013.0	−0.9	−24.6	−124
09/11/2020	DZN-1	−12.7694	45.2877	DZIANI	85.8	bdl	39700.0	9.1	0.5	bdl	958.0			
09/11/2020	DZN-3	−12.7694	45.2877	DZIANI	bdl	bdl	283500.0	64.5	2.6	24.0	7823.0		−24.8	−141
09/11/2020	DZN-3-dupl	−12.7694	45.2877	DZIANI										
09/11/2020	INGV-01	−12.7710	45.2903	DZIANI	0.2	6.0	81900.0	73.6	16.5	39.0	478.0	−6.3	−38.4	−184
09/11/2020	DZE-2	−12.7710	45.2903	DZIANI	0.3	1.2	3897.0	77.6	20.6	3.8	9.0			

Table 1b. Isotopic values of the noble gases from bubbling area at Petite Terre (surveys 2018–2020)

Sampling date	Sample	Lat	Long	Site	Noble gases isotopes											
					R/R_a	$^4He/^{20}Ne$	[^{4}He] (ppm)	[^{20}Ne] (ppm)	R_c/R_a	^{40}Ar (ppm)	^{38}Ar (ppm)	^{36}Ar (ppm)	^{40}Ar* (ppm)	^{40}Ar (atm)	$^{40}Ar/^{36}Ar$ (corr)	$^{38}Ar/^{36}Ar$ (corr)
08/11/2020	OVPF-1	−12.8002	45.2874	BAS	5.86	199.45	28.25	0.14	5.87	110.71	0.06	0.31	18.86	91.85	355.50	0.19
08/11/2020	C1a1-glass	−12.8002	45.2874	BAS												
08/11/2020	OVPF-2	−12.8002	45.2874	BAS	5.92	136.09	24.49	0.18	5.94	91.41	0.05	0.25	18.86	72.55	371.61	0.19
08/11/2020	C2a2-glass	−12.8002	45.2874	BAS												
08/11/2020	OVPF-3	−12.8002	45.2895	BAS	5.54	108.44	19.72	0.18	5.55	90.47	0.05	0.26	13.30	77.17	345.67	0.19
08/11/2020	GD-1	−12.8002	45.2895	BAS												
08/11/2020	OVPF-4	−12.8002	45.2895	BAS	5.46	78.22	19.89	0.25	5.48	98.17	0.05	0.29	13.31	84.86	341.19	0.19
08/11/2020	GD-2	−12.8002	45.2895	BAS												
10/11/2020	C1-b1	−12.8002	45.28736	BAS	5.53	99.83	26.99	0.27	5.55	72.16	0.03	0.18	19.54	52.62	404.40	0.19
10/11/2020	C1-b2	−12.8002	45.28736	BAS	5.55	237.19	31.63	0.13	5.56	87.63	0.04	0.23	18.54	69.08	373.95	0.19
08/09/2019	Dist N	−12.8006	45.28883	BAS	6.86	329.38	24.41	0.07	6.87	59.28	0.03	0.15	14.92	44.36	392.00	0.19
08/09/2019	Dist N	−12.8006	45.28883	BAS	6.94	261.61	25.05	0.10	6.95	55.17	0.02	0.13	16.35	38.82	418.02	0.19
08/09/2019	C1-2	−12.8002	45.28736	BAS	7.23	529.11	27.50	0.05	7.24	62.81	0.03	0.14	20.24	42.56	434.13	0.19
08/09/2019	C1-2	−12.8002	45.28736	BAS	7.12	152.41	26.03	0.17	7.14	125.30	0.07	0.36	19.62	105.68	348.11	0.19
13/09/2019	Dist 2	-12.8005	45.28871	BAS	7.19	310.71	25.67	0.08	7.20	72.00	0.04	0.19	15.38	56.63	374.36	0.19
08/09/2019	DIST-1	−12.8006	45.28883	BAS	6.90											
08/09/2019	C1-2	−12.8002	45.28736	BAS	7.17											
06/04/2019	Dist 1-A	−12.8006	45.28883	BAS	7.07	167.74	21.20	0.13	7.08	87.28	0.05	0.24	15.06	72.22	354.85	0.19
06/04/2019	Dist 1-B	−12.8006	45.28883	BAS		1663.88										
06/04/2019	Dist 2	−12.8005	45.28871	BAS												
06/04/2019	C1-1	−12.8002	45.28736	BAS	7.52	219.30	22.48	0.10	7.53	105.50	0.06	0.30	16.16	89.34	347.41	0.18
06/04/2019	C1-3	−12.8002	45.28736	BAS	7.26	138.87	22.47	0.16	7.27	141.91	0.08	0.43	15.90	126.01	331.79	0.19
06/04/2019	MAR 3	−12.8005	45.28740	BAS	7.24	107.84	27.16	0.25	7.26	238.96	0.14	0.75	17.44	221.52	318.11	0.19
16/12/2018	MAR-1	−12.8004	45.28766	BAS	3.24	1.07	8.20	7.65	4.18	3346.63	2.15	11.53	-	-	290.73	0.19
16/12/2018	MAR-1	−12.8004	45.28766	BAS												
16/12/2018	CI-1a	−12.8002	45.28736	BAS												
16/12/2018	C1-b	−12.8002	45.28736	BAS	7.13	200.34	23.19	0.12	7.14	75.08	0.04	0.19	18.51	56.57	390.28	0.19
16/12/2018	CI-1	−12.8002	45.28736	BAS												
16/12/2018	MAN-1	−12.8006	45.28705	BAS	6.40	222.22	102.00	0.46	6.41	497.76	0.26	1.41	81.33	416.43	352.77	0.19
16/12/2018	MAN-1	−12.8006	45.28705	BAS												
16/12/2018	MAN-2	−12.8006	45.28705	BAS	6.93	43.59	113.25	2.60	6.97	1762.78	1.07	5.71	74.57	1688.20	308.79	0.19
16/12/2018	MAN-2	−12.8006	45.28705	BAS												
09/11/2020	OVPF-5	−12.7708	45.2858	DZIANI	5.82	54.00	42.51	0.79	5.85	405.89	0.24	1.24	39.52	366.37	326.89	0.19
09/11/2020	DZW-1	−12.7708	45.2858	DZIANI	5.28	48.62	42.45	0.87	5.31	281.37	0.16	0.85	31.40	249.97	331.99	0.19
09/11/2020	DZW-4	−12.7708	45.2858	DZIANI	6.82	577.25	2322.33	4.02	6.83	9088.27	4.72	25.11	1669.59	7418.68	362.06	0.19
09/11/2020	DZW4-dupl	−12.7708	45.2858	DZIANI	6.74	575.22	2438.49	4.24	6.74	9634.94	5.01	26.56	1786.22	7848.72	362.81	0.19
09/11/2020	OVPF-6	−12.7694	45.2877	DZIANI	6.67	628.12	1139.54	1.81	6.67	2055.13	0.82	4.42	749.02	1306.11	463.77	0.19
09/11/2020	DZN-1	−12.7694	45.2877	DZIANI												
09/11/2020	DZN-3	−12.7694	45.2877	DZIANI	6.42	1994.54	8223.72	4.12	6.42	15342.65	6.07	32.85	5636.66	9705.99	467.01	0.18
09/11/2020	DZN-3-dupl	−12.7694	45.2877	DZIANI	6.42	2122.31	8439.59	3.98	6.42	15764.01	6.22	33.62	5828.82	9935.20	468.76	0.19
09/11/2020	INGV-01	−12.7710	45.2903	DZIANI	6.39	33.31	620.22	18.62	6.44	12340.99	7.63	40.26	444.49	11896.50	306.44	0.19

acquisition operations, or are referable to emission sources that underwent secondary processes that altered their initial elemental and/or isotopic composition. In what follows, we will attempt to provide a description of these samples as well, however they will no longer be taken into account in the interpretative considerations (and related graphs).

3.1. *Gas composition*

With the exception of one CH_4-rich bubbling spot in the Dziani Dzaha Lake (DZE), all studied samples of

Table 1c. Corrected data for air contamination from the samples listed in Table 1a (surveys 2018–2020)

Sampling date	Sample	Lat	Long	Site	Corrected for air contamination						
					He (ppm)	H_2 (ppm)	O_2%	N_2%	CH_4 (ppm)	CO (ppm)	CO_2%
08/11/2020	OVPF-1	−12.8002	45.2874	BAS	26.47	18.34	0.00	0.24	3932.82	0.81	99.37
08/11/2020	C1a1-glass	−12.8002	45.2874	BAS	20.30	6.85	0.00	−0.46	3949.21	2.28	100.07
08/11/2020	OVPF-2	−12.8002	45.2874	BAS	23.53	17.42	0.00	0.04	3881.17	0.61	99.57
08/11/2020	C2a2-glass	−12.8002	45.2874	BAS	−31.26	270.09	0.00	29.85	1112.06	89.66	70.00
08/11/2020	OVPF-3	−12.8002	45.2895	BAS	20.27	83.16	0.00	0.33	5365.96	36.51	99.11
08/11/2020	GD-1	−12.8002	45.2895	BAS	12.90	6.93	0.00	−0.38	5033.43	2.78	99.88
08/11/2020	OVPF-4	−12.8002	45.2895	BAS	19.26	221.11	0.00	0.38	5218.42	0.00	99.07
08/11/2020	GD-2	−12.8002	45.2895	BAS	15.62	3.03	0.00	0.81	4825.20	−0.09	98.70
10/11/2020	C1-b1	−12.8002	45.28736	BAS	28.60	28.63	0.00	0.27	4047.28	0.00	99.32
10/11/2020	C1-b2	−12.8002	45.28736	BAS	26.17	0.00	0.00	0.04	3936.47	0.00	99.57
08/09/2019	Dist N	−12.8006	45.28883	BAS	25.62	0.00	0.00	0.15	2925.35	0.00	99.56
08/09/2019	Dist N	−12.8006	45.28883	BAS	26.22	112.99	0.00	0.29	3008.39	0.00	99.39
08/09/2019	C1-2	−12.8002	45.28736	BAS	29.26	0.00	0.00	0.12	2467.35	0.00	99.63
08/09/2019	C1-2	−12.8002	45.28736	BAS	28.62	16.36	0.00	0.22	2438.25	0.00	99.53
13/09/2019	Dist 2	−12.8005	45.28871	BAS	27.39	0.00	0.00	−0.06	2958.37	1.22	99.76
08/09/2019	DIST-1	−12.8006	45.28883	BAS							
08/09/2019	C1-2	−12.8002	45.28736	BAS							
06/04/2019	Dist 1-A	−12.8006	45.28883	BAS	21.57		0.00	−0.12	2512.60	1.23	99.87
06/04/2019	Dist 1-B	−12.8006	45.28883	BAS	20.74		0.00	−0.26	2531.98	2.50	100.01
06/04/2019	Dist 2	−12.8005	45.28871	BAS	19.47		0.00	−0.07	2469.39	2.15	99.82
06/04/2019	C1-1	−12.8002	45.28736	BAS	23.61		0.00	0.01	2148.01	2.16	99.77
06/04/2019	C1-3	−12.8002	45.28736	BAS	23.56		0.00	0.14	2090.69	5.13	99.65
06/04/2019	MAR 3	−12.8005	45.28740	BAS	27.74		0.00	0.22	2809.43	10.31	99.49
16/12/2018	MAR-1	−12.8004	45.28766	BAS	8.10	3.18	0.00		1910.79	2.39	100.01
16/12/2018	MAR-1	−12.8004	45.28766	BAS							
16/12/2018	CI-1a	−12.8002	45.28736	BAS			0.00		1483.76	6.87	102.53
16/12/2018	C1-b	−12.8002	45.28736	BAS	23.32	322.78	0.00	0.38	2162.05	1.72	99.37
16/12/2018	CI-1	−12.8002	45.28736	BAS							
16/12/2018	MAN-1	−12.8006	45.28705	BAS	109.57		0.00	1.72	4699.48	0.71	97.80
16/12/2018	MAN-1	−12.8006	45.28705	BAS							
16/12/2018	MAN-2	−12.8006	45.28705	BAS	127.26		0.00	2.27	5378.54	9.27	97.18
16/12/2018	MAN-2	−12.8006	45.28705	BAS							
09/11/2020	OVPF-5	−12.7708	45.2858	DZIANI	44.00	11.86	0.00	−1.28	5089.07	−0.02	100.76
09/11/2020	DZW-1	−12.7708	45.2858	DZIANI	39.50	8.34	0.00	−2.26	5044.09	0.30	101.75
09/11/2020	DZW-4	−12.7708	45.2858	DZIANI							
09/11/2020	DZW4-dupl	−12.7708	45.2858	DZIANI							

(continued on next page)

Table 1c. (continued)

Sampling date	Sample	Lat	Long	Site	Corrected for air contamination						
					He (ppm)	H_2 (ppm)	O_2%	N_2%	CH_4 (ppm)	CO (ppm)	CO_2%
09/11/2020	OVPF-6	−12.7694	45.2877	DZIANI	1043.35	12.35	0.00	7.64	38935.48	0.00	88.36
09/11/2020	DZN-1	−12.7694	45.2877	DZIANI	984.77	−0.01	0.00	7.63	40814.10	−0.01	88.19
09/11/2020	DZN-3	−12.7694	45.2877	DZIANI							
09/11/2020	DZN-3-dupl	−12.7694	45.2877	DZIANI							
09/11/2020	INGV-01	−12.7710	45.2903	DZIANI	2301.87	187.42	0.00	59.24	397823.18	28.19	0.73
09/11/2020	DZE-2	−12.7710	45.2903	DZIANI	257.75	219.69	0.00	54.91	260997.01	63.93	18.94

Table 1d. Chemical composition of major and minor gaseous components from bubbling area at Petite Terre (survey 2021)

Sampling date	Sample	Lat	Long	Site	Major (Raw)						
					CO_2 (vol%)	CO (ppmv)	CH_4 (ppmv)	N_2 (vol%)	O_2 (vol%)	H_2 (ppmv)	He (ppmv)
5/9/2021	C1-2	−12.800117	45.2873	BAS	97.7	0.8	5099	0.25	0.0705	bdl	22
5/9/2021	C1-1	−12.80015	45.28736	BAS	97.45	0.9	5158	0.68	0.27	bdl	2021
5/9/2021	MAN	−12.80064	45.28705	BAS	96.94	1.5	6654	1.59	0.45	bdl	38
5/9/2021	MAR	−12.80045	45.28873	BAS	97.73	0.9	5838	0.43	0.23	bdl	15
5/9/2021	DIST	−12.799917	45.28612	BAS	97.62	1.4	6637	0.5	0.24	bdl	2021
7/9/2021	DZW	−12.770833	45.28582	DZIANI	97.28	1.1	6126	1.2021	0.73	bdl	54
7/9/2021	DZN	−12.769403	45.28771	DZIANI	89.71	1	24,400	6.5	1.98	bdl	330

Table 1e. Corrected data for air contamination from the samples listed in Table 1d (survey 2021)

Sampling date	Sample	Lat	Long	Site	Corrected for air contamination						
					He (ppm)	H_2 (ppm)	O_2%	N_2%	CH_4 (ppm)	CO (ppm)	CO_2%
5/9/2021	C1-2	−12.800117	45.2873	BAS	22.384		0.07	0.254368318	5188.096214	0.814	99.2
5/9/2021	C1-1	−12.80015	45.28736	BAS	21.34		0.27	0.691000802	5241.444318	0.9146	98.5
5/9/2021	MAN	−12.80064	45.28705	BAS	37.834		0.45	1.583044892	6624.89353	1.4934	97.3
5/9/2021	MAR	−12.80045	45.28873	BAS	15.172		0.23	0.434934814	5904.998706	0.9103	98.7
5/9/2021	DIST	−12.799917	45.28612	BAS	21.28		0.24	0.506657787	6725.375469	1.4186	98.6
7/9/2021	DZW	−12.770833	45.28582	DZIANI	58.525		0.79	1.311395671	6639.347007	1.1922	97.2
7/9/2021	DZN	−12.769403	45.28771	DZIANI	1026		6.16	20.20949473	75863.33407	3.1092	65.9

the Mayotte gas seeps are CO_2-dominated. The Mayotte noble gas show a more variable composition for the Dziani Dzaha Lake than for the Airport tidal flat (BAS; Tables 1a–1e), with ^{4}He ranging between 8.2 and 113 ppm at BAS and between 42.5 and 1139.5 for the Dziani Dzaha Lake. The ^{20}Ne values for the BAS zone range from 0.1 to 7.7 ppm and between 0.8 and 18.6 for the Dziani Dzaha Lake. Finally, the ^{40}Ar is in the range 55.2–3346.6 ppm in BAS and 281.4–2055.1 for the Dziani Dzaha Lake. Some of the samples in both Dziani and BAS areas have a significant air contamination showing concentrations of N_2 and O_2 up to 76.4% and 20.4% respectively (Tables 1a–1e, Figure 2a).

The BAS bubbling gases from the tidal flat show a CO_2 dominated composition with concentrations up to 98.8% and a variable concentration in CH_4 ranging between 16 and 5291 ppm with the lowest value

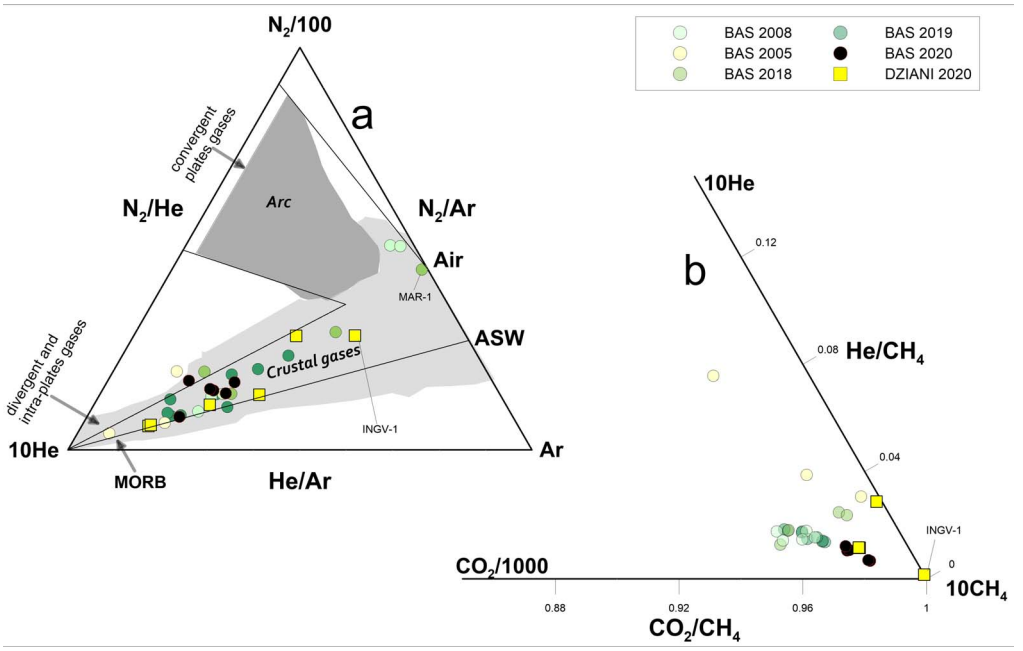

Figure 2. Relative proportion of He–Ar–N_2 in Mayotte bubbling gases (a); the fields of composition of gases emitted in crustal and arc settings are also shown. Data collected at Petite Terre show variable degrees of air and ASW contamination. In (b) CO_2–CH_4–He ternary diagram shows that the CO_2-rich Mayotte gases contain a significant amount of CH_4 with the highest proportion of methane recorded in the Dziani Dzaha Lake. Areas in different shades of grey distinguish gases from arc- and crustal geodynamic environments—from literature data.

related to an air-contaminated sample (C_2a_2-glass). The BAS gases show low concentrations in H_2 and CO, ranging from below detection limit to 11 ppm for H_2 and to 18 ppm for CO (higher values for H_2 and CO in Tables 1a–1e refer to samples collected in steel samplers, which we do not consider reliable, as discussed in Section 4.3). At the Dziani Dzaha Lake, CO_2 is also the dominant gas species in two of the three analyzed spots (DZW, DZN), with values up to 97.3%, while CH_4 is variable between 3897 and 81,900 ppm, except in the third spot (DZE) where CH_4 is the dominant gas. The H_2 and CO are generally present in low concentrations.

The chemical composition of the Mayotte gases plotted in a N_2, He and Ar ternary diagram (Figure 2a) follows a mixing trend between a He-rich component and an atmospheric component (air or air-saturated water—ASW). The bubbling gases from both areas at Mayotte show a variable degree of contamination by an atmospheric end-member, and its contribution is probably slightly higher for air than for ASW at least in BAS. On the whole, the He–Ar–N_2 variability falls within a typical compositional range of gases emitted in intraplate or extensive tectonic settings. The two dominant mixing sources appear to be atmospheric and MORB-type mantle, and they are distinct from typical subduction-related gases, which have higher N_2/Ar ratios due to the N_2 excess released to the wedge by subducting sediments [e.g., Barry and Hilton, 2016]. With regard to the helium variability, the similarity between Dziani Dzaha Lake and BAS is interesting, as there seems to be no appreciable difference in the air-MORB mixing trends. This suggests that shallow processes do not significantly affect helium abundances at Petite Terre.

The chemical composition in relation to the plot of CO_2–CH_4–He (Figure 2b) highlights that low temperature gas seeps of Petite Terre have a general high CH_4 concentration. A relatively higher abundance of CH_4 in Dziani than in BAS tidal flat is likewise

evident. Since the beginning of the seismo-volcanic crisis, the CO_2-rich bubbling spots of the two sites show comparable abundances of CH_4, and Dziani still hosts the only CH_4-dominated bubbling area. The INGV-1 sample in Dziani is the most enriched in methane (Figure 1c); however, it should also be noted that this specific sample is also affected by air contamination.

3.2. *Systematics of noble gas isotope ratios,* CO_2 *and* CH_4 *isotopes*

Tables 1a–1e report the isotopic compositions of noble gases, CO_2 and CH_4 in the sampled gases from the two bubbling areas of Petite Terre. Regarding the measured $^3He/^4He$ ratios, these vary between 5.45 and 7.5 R_a in BAS, and between 5.3 and 6.8 R_a in Dziani Dzaha Lake (Figure 3). It is worth noting that the range of R/R_a values is very similar between BAS and Dziani, although it should be noted that less data is available for Dziani and that they are only related to the 2020 campaign. In both BAS and Dziani, a few samples show a clear air contamination as recorded by relatively high content of N_2 and O_2. It is possible that these samples underwent some issues during the sampling operations or during the storage and transport to the laboratory that fractionated the $^3He/^4He$, (for example MAR-1 Figure 3) leading us to exclude them for further discussion. The majority of samples do not show significant air contamination as indicated by both the chemistry of gases and the noble gas systematics (Tables 1a–1e). For instance, the $^4He/^{20}Ne$ ratios is at least 2 orders of magnitude higher than the ratio in air (0.318) reaching 1663 in the BAS (this study) and up to 2750 in the survey carried out by BRGM in 2008 [Sanjuan et al., 2008], while is reaches up to 2122 in the Dziani Dzaha Lake.

The $^{40}Ar/^{36}Ar$ values range from the atmospheric ratios up to 434 in BAS, and up to 468 in the Dziani Dzaha Lake. The few air contaminated samples have lower ratios, like MAR-1 and MAN-2 in BAS site ($^{40}Ar/^{36}Ar$ = 290 and 308; and $^4He/^{20}Ne$ = 1.07 and 43.59, respectively), and INGV-01 in the Dziani Dzaha Lake ($^{40}Ar/^{36}Ar$ = 306 and $^4He/^{20}Ne$ = 33.3).

With the exception of a few air-contaminated samples, the difference between R/R_a and R_c/R_a is almost negligible.

The $^4He/^{40}Ar^*$ ratio of BAS gases ranges between 1.3 and 1.7, with a general overlap of values between

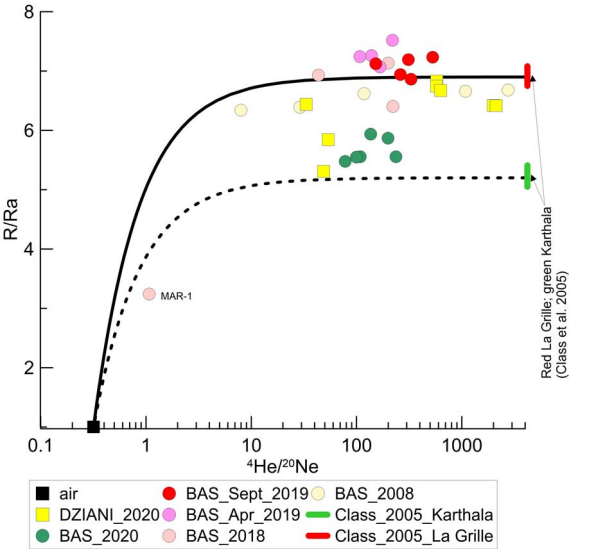

Figure 3. $^4He/^{20}Ne$ versus $^3He/^4He$ (R/R_a) ratios in Mayotte bubbling gas. Continuous and dashed black lines correspond to mixing trend between air and magmatic gases. Magmatic signature is constrained using the analyses of mineral crushing of Class et al. [2005] from La Grille and Karthala volcanoes [see also Liuzzo et al., 2021]. The two solid red and green bars correspond to the range of the R/R_a variability in La Grille and Karthala datasets [Class et al., 2005]. La Grille is the older and rarely active volcano in the north of Grande Comore (last dated eruption: 1029–1424 CE) [Bachèlery and Hémond, 2016, and references therein], while Karthala is the most active volcano of Grande Comore (last eruption: 2007).

different sampled pools and sampling periods, and they are within 1.1 and 1.5 in Dziani Dzaha Lake, irrespective of the variable CH_4/CO_2 ratios. These values fall within the typical range of mantle production ratio [$^4He/^{40}Ar^*$ = 1–5; Marty, 2012] and magmatic values from other geodynamic settings [e.g., Reunion hot spot, Boudoire et al., 2018; Eger Rift intra-plate in Europe, Bräuer et al., 2011; Etna intra-plate, Paonita et al., 2012; Kolumbo arc volcano in Greece, Rizzo et al., 2019].

The $^4He/^{40}Ar^*$ variability is commonly used to track magmatic degassing processes due to the ~7–10 times lower solubility in silicate melts of Ar

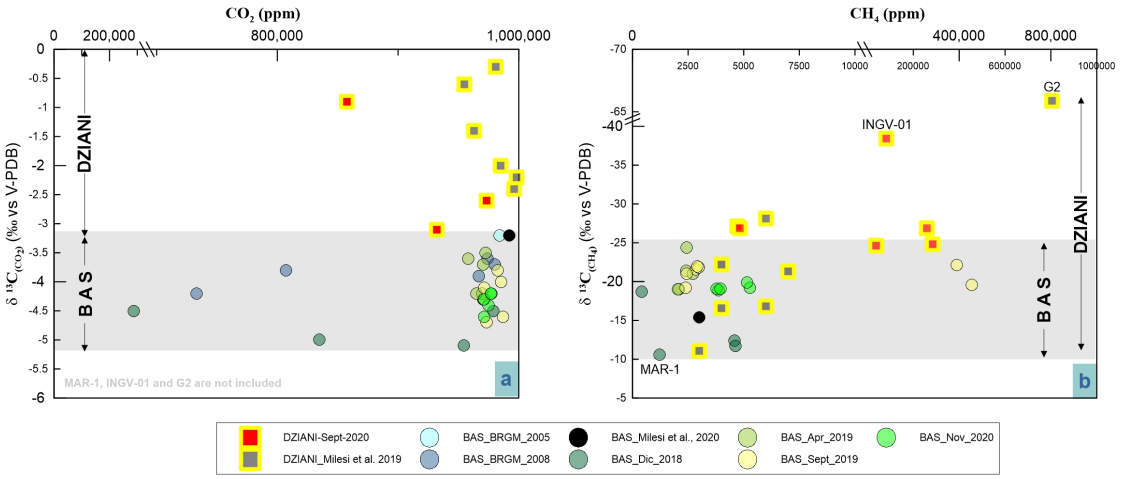

Figure 4. Comparison of carbon isotopic variability in CO_2 (left) and CH_4 (right) and elemental composition of the two main bubbling areas of Mayotte–Petite Terre (BAS tidal flat and Dziani Dzaha intracrateric lake).

than He [e.g. Burnard, 2001, Paonita et al., 2012, Barry et al., 2014, Boudoire et al., 2018]. $^4He/^{40}Ar^*$ ratios at Petite Terre do not show systematic variations as a function of location or time. Liuzzo et al. [2021] suggest that this homogeneous signature reflects that all bubbling spots are related to a single degassing source and pressure, likely related to magmas stored close to the mantle-crust underplating depth (15–20 km depth), as observed in other magmatic systems [e.g., Reunion, Boudoire et al., 2018]. This depth range corresponds to the shallower part of the magmatic plumbing system below Mayotte, where evolved basanitic magma differentiate to form phonolitic melts [Berthod et al., 2021a,b, Foix et al., 2021].

The C-isotope compositions of CO_2 ($\delta^{13}C_{CO_2}$) at BAS gases vary from −5.7‰ and −3.5‰, where the most negative ratios are those measured in samples from MAN-1 and MAN-2 a sampling pool with relatively low gas flux and located close to a dense area of Mangrove trees on the airport flat. At Dziani Dzaha Lake the variability is much wider with $\delta^{13}C_{CO_2}$ spanning between −0.9 and −6.3‰ (data from this work), where the most negative value is that of the sample INGV-01 from the CH_4-rich plume (DZE). Interestingly, previous data collected in 2016 from Milesi et al. [2019] show an even higher variability with $^{13}C_{CO_2}$ between −0.3 and −20.1, where the most negative correspond to G2 sample in Milesi et al. (2019) collected in the same area of DZE. Figure 4a shows the $\delta^{13}C_{CO_2}$ distribution and highlights a significant separation of the C isotope signature between the two bubbling areas, where Dziani is systematically more positive than BAS (with the exception of G2 not represented in the plot) and where the $\delta^{13}C_{CO_2}$ in BAS are confined to a narrow range of about 2 delta units.

On the contrary, the distribution of the C-isotope composition of CH_4 ($\delta^{13}C_{CH_4}$) (Figure 4b) partly overlaps in BAS and Dziani areas, with the BAS site showing again a fairly narrow range of variability, (from −25‰ to −10‰). At BAS, the least negative values are found in the MAN low-flux pool located close to the mangrove area (MAN-1 and MAN-2 samples) that is considered affected by gas–water dissolution by Liuzzo et al. [2021]. The site of Dziani Dzaha Lake shows a wider variation in $\delta^{13}C_{CH_4}$ fluctuating from minimum values of more than −65‰ (DZE area) to maximum values of −11‰ (DZW area). The different isotopic variability of carbon in a $\delta^{13}C_{CO_2}$ and $\delta^{13}C_{CH_4}$ space is evident in Figure 5, where the two markers are linearly and negatively correlated (R^2 = 0.7) in the BAS site and positively correlated in the Dziani Dzaha Lake. Interestingly our new dataset on the Dziani Dzaha Lake clearly shows more negative $\delta^{13}C_{CH_4}$ values with respect to that

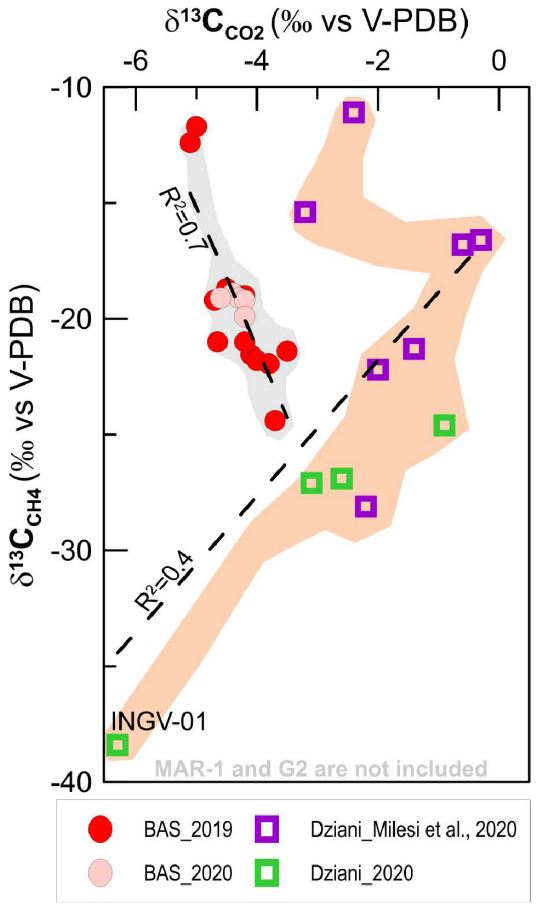

Figure 5. Carbon isotopic composition in CO_2 and CH_4 in the two gas seeps areas of Mayotte (BAS tidal flat and Dziani Dzaha Lake). Milesi et al. [2020] data were collected in 2016, before the beginning of the seismo-volcanic crisis in 2018.

of Milesi et al. [2020]. Regarding hydrogen isotopic values in CH_4 (δD_{CH_4}), our samples yielded a δD of -118.1‰ and -137.8‰ V-SMOW, respectively in BAS and -124‰ and -184‰ V-SMOW in Dziani.

4. Discussion

4.1. CO_2 *origin and gas–water interaction*

In order to assess the origin of CO_2 rich gas emissions in Mayotte, we followed the approach used in Sano and Marty [1995] and we extended the dataset from the BAS area discussed in Liuzzo et al. [2021] with new gas sampling made in 2020 in BAS and in the Dziani Dzaha Lake. In order to discriminate the possible contributions from various sources (magmatic, organic and marine sediments), we considered the isotopic variability of carbon in CO_2 versus $CO_2/^3He$ ratio (Figure 6). The two mixing curves were modeled between the local mantle endmember resulting from the average values of our data (in which we only considered data that were not modified by secondary processes), data from literature [$CO_2/^3He = 5.0 \times 10^9$ and $\delta^{13}C = -4.3$‰, Liuzzo et al., 2021] and an organic ($\delta^{13}C = -25$‰) and limestone endmember ($\delta^{13}C = 0$‰) from Hoefs [2015]. For both organic and limestone carbon endmembers, a value of $CO_2/^3He = 1.0 \times 10^{13}$ is assumed. Finally, in order to evaluate the secondary processes of gas–water interaction, we have considered data corrected for air only for samples having $N_2 < 22\%$, following the approach of Liuzzo et al. [2021].

The distribution of the data for the two degassing areas at Petite Terre shows clear differences. With the exception of the MAN-1 and MAN-2 samples, the BAS area shows little variability in bulk chemistry and C isotopy and are reasonably interpretable as being related to an outgassing process from a deep magmatic source. Conversely, the gas samples from the Dziani Dzaha Lake area have a larger scattering.

Gas–water interaction effects previously highlighted for some samples from the BAS area by Liuzzo et al. [2021] likely play an even more important role in the Dziani Dzaha Lake. We modeled four possible Rayleigh fractionation curves by assuming gas dissolution in water under equilibrium conditions (Appendix A, Equation (A3)). However, whereas in the case of the BAS zone a simple dissolution process can be assumed (MAN 1-2 curve Rf-1) [Liuzzo et al., 2021], in the case of Dziani, a single dissolution step cannot reproduce the measured large scattering. Moreover, when considering the typical parameters of the Dziani Dzaha Lake (pH = 9 and temperature of 36 °C from Milesi et al. [2020]) the corresponding curve Rf-2 clearly does not fit with any Dziani Dzaha Lake data. The pH value of up to 9 in Diazni Dzaha Lake can potentially facilitate calcite precipitation. However, the precipitation of calcite, by subtracting the heavier isotope, would produce a more negative $\delta^{13}C$ component in the gas phase (resulting in a curve that would overlap with Rf-2), but in our case the trend of the values measured in the lake is the

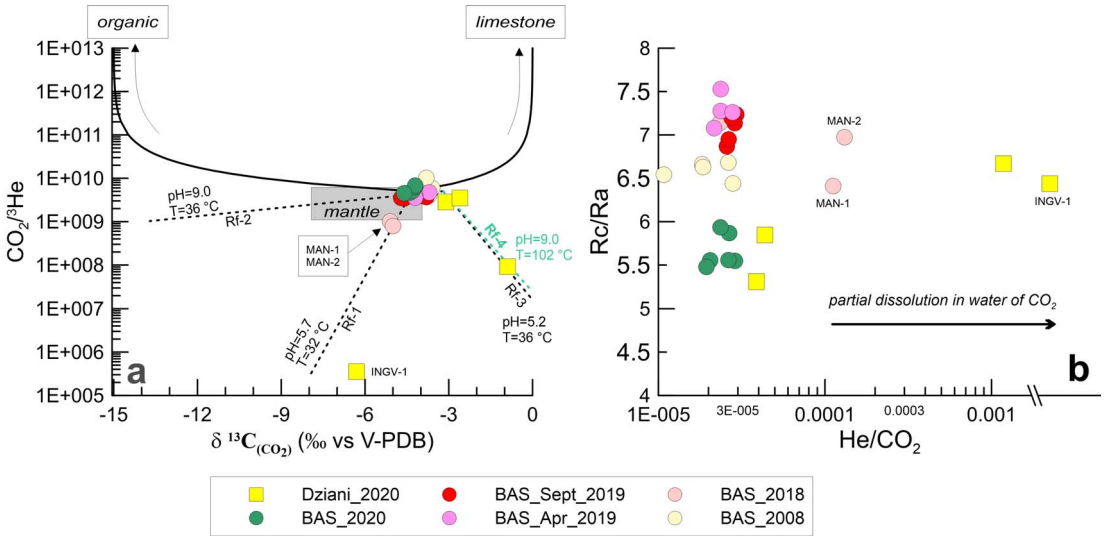

Figure 6. In (a) δ^{13}C of CO_2 versus $CO_2/^3$He diagram of bubbling gases at Petite Terre (Mayotte). In (b) He/CO_2 versus R_c/R_a. Diagram 6a shows that gases at Petite Terre are in the field of mantle-like sources with no evident organic or limestone contributions. Solid lines are mixing curves between organic, mantle and limestone endmembers. The dashed lines indicates Rayleigh fractionation (Rf) trends related to gas dissolution in water under four different pH–T conditions (see text for discussion and interpretation). Diagram 6b displays the effect of variable degree of water-gas interaction controlling CO_2/He variability.

opposite. In order to fit the Dziani Dzaha Lake gases in the range of temperatures of 32–36 °C, much more acid pH of about 5.2–5.7 are needed (Rf-3 path). If, on the other hand, fractionation in equilibrium with the lake's pH of about 9 is considered, the temperature required to obtain a good fit on the data (Rf-4 path) should be about 102 °C. However, these high temperatures are not realistic, nor have such temperature anomalies ever been found in any of the surveys performed in the lake before or after the beginning of the seismic crisis. Modeling seems to suggest that simple fractionation does not occur in the water column of the Dziani Dzaha Lake, on the other hand if the fractionation process occurs in the aquifer and does not undergo major changes in the lake, the Rf-3 model is likely the most plausible.

Nevertheless, the variability of He/CO_2 versus R_c/R_a shown in Figure 6b, evidences that a partial dissolution in water did play a role in modifying the composition of gas bubbling streaming through the Dziani Dzaha Lake, and appears to be notably extreme in the CH_4-rich INGV-1 sample. In particular, this sample is collected in correspondence of the deepest portion of the lake (Figure 1c), and as already noted for sample G2 in Milesi et al. [2020], may have been significantly affected by the gas transfer and residence in the higher water column.

The current dataset does not permit to exclude that gaseous emissions from Dziani Dzaha Lake undergo gas–water interaction processes under non-equilibrium conditions and/or the occurrence of other fractionation processes than those here modeled. Among these, isotope exchange in Dziani between $\delta^{13}C_{CO_2}$ and $\delta^{13}C_{TDIC}$ could lead to the less negative isotopic values measured at the Dziani Dzaha Lake with respect to BAS, if we consider that water lake reaches DIC concentrations up to 0.2 mol/L and $\delta^{13}C_{TDIC}$ up to +13‰ [Cadeau et al., 2020]. The acquisition of more data on both exsolved and dissolved gases in the future is thus needed in order to better constrain the processes controlling the variability of the carbon isotopic signature in the Dziani Dzaha Lake. All of these effects need to be evaluated and eventually filtered out in order to calculate the thermobarometric conditions of the hydrothermal system feeding the gas seeps (see next

section), as it has been recognized in other studies of hydrothermal gases [Capasso et al., 2005, Gilfillan et al., 2009, Rizzo et al., 2019]. In fact, besides $\delta^{13}C$ isotopic signature, the $CO_2/^3He$, He/CO_2, CH_4/CO_2 ratios can also be potentially modified by oxydation/reduction reactions and/or by gas–water interaction in which CO_2 dissolves preferentially with respect to the other species.

4.2. CH_4 *origin and* $\delta^{13}C$ *versus* δ^2H *variability*

For the samples collected in the 2019–2020 campaigns, it was possible to define the isotopic signature of carbon and hydrogen in methane in both BAS and the Dziani Dzaha Lake sites and compare them with previous data of Dziani Dzaha Lake from Milesi et al. [2020]. The results are plotted in the classification diagram proposed by Schoell [1980] (Figure 7). It must be stressed that distinguishing between methanogenesis processes of biological origin and thermogenic processes at the origin of CH_4 [Mazzini et al., 2011, Schoell, 1980, Welhan, 1988] is complicated by the possible mixing between endmembers with different isotopic signatures [Taran et al., 2010a,b], or by the occurrence of oxidation processes [e.g., Batista Cruz et al., 2019].

Although with some relative variability, the isotopic signature of methane in BAS falls in the field of abiogenic origin, together with sample G7, acquired in 2016 in this area by Milesi et al. [2020]. This confirms that outgassing in the BAS tidal area originates from a homogeneous and unique source, particularly if we also take into account the stable and low variability of R_c/R_a and $\delta^{13}C$-CO_2 values (Figures 3–5). The situation in the Dziani Dzaha Lake is more complex. The CH_4-rich G_2 sample collected near the deepest part of the lake corresponds to a gas that has clearly undergone a reduction process by microbial methanogenesis, as already highlighted in Milesi et al. [2020]. Our INGV-01 sample from this area (Tables 1a–1e), records a possible strong interaction in water or in the sediments (Figure 6b). The isotopic characteristics of methane for this sample can be consistent with a thermogenic origin or with mixing between abiogenic and biogenic endmembers. In the Dziani Dzaha Lake, the isotopic signature of the CH_4-rich bubbling is thus distinct from that of the CO_2-rich bubbling (ex. G3), which have abiogenic signature similar to the samples in BAS, but with a less negative proportion of δ^2H. The remaining samples from the 2020 campaign in Dziani have a signature intermediate between abiogenic and thermogenic fields (DZN 1-2; OVPF-5; DZW 1-4). The variability of methane isotopic characteristics in distinct outgassing areas in Dziani thus appears to be much more complex than measured in BAS, which is confirmed also by the wider variability in $\delta^{13}C$ signature in CO_2 (Figures 4, 5). This again suggests that several processes may operate in the lake, including abiotic degassing of gases, microbial production and oxidation of methane, and partial dissolution of CO_2 in water, all of which contribute to varying degrees to the greater chemical and isotopic variability compared to the more homogeneous BAS area.

It is therefore clear that further data are needed to better constrain the origin of methane in the Dziani Dzaha Lake, and we are aware that the debate on methane origin is open within the scientific community, in particular in order to justify its possible abiotic origin assuming a “magmatic” or “late magmatic” origin [Etiope and Sherwood Lollar, 2013]. However, answering this question is not trivial, considering that the recent submarine eruption only 50 km off-shore from Petite Terre represents by far the largest known submarine eruption until now and that intense seismicity occurs at variable distance from the island [Feuillet et al., 2021, Berthod et al., 2021a,b, Foix et al., 2021]. In this context, a further clue is given by the isotopic signature of helium involved in the outgassing process at Petite Terre, which can be useful in discerning and assessing the deep origin of the gas. Therefore, we considered the isotopic variability of methane by comparing it with the percentage of mantle-related helium, following the approach indicated in Etiope and Sherwood Lollar [2013] (Figure 8). In our case, the Petite Terre gases fall within the area where magmatic CH_4 inputs are clearly recognized (EPR—East Pacific Rise, Socorro, Lost City [Proskurowski et al., 2008, Taran et al., 2010a, Welhan and Craig, 1983]). This leads us to conclude that input of gas of magmatic origin contributes to the general outgassing at Petite Terre, and specifically even regarding a not negligible contribution of methane, which in turn, particularly in the Dziani Dzaha Lake area, has undergone further transformation processes by microbial activity.

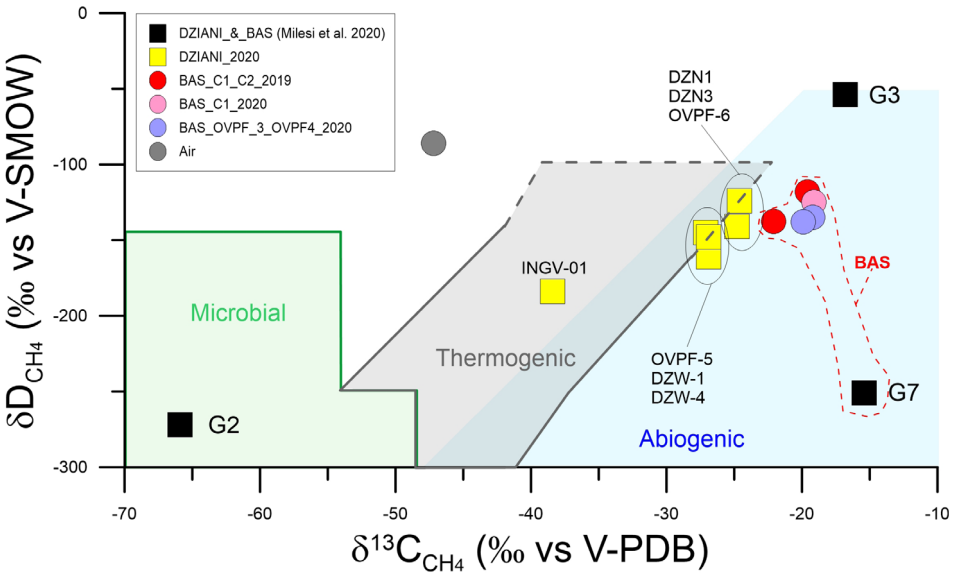

Figure 7. $\delta^{13}C_{CH_4}$ versus δD_{CH_4} classification diagram (modified from Schoell [1980]). G2, G3 and G7 data acquired in 2016 from Milesi et al. [2020]. Most samples collected in the Mayotte gas seeps fall in the typical abiogenic fields, while a clear microbial signature is found in the sample collected by Milesi in 2016. The sample INGV-01 collected in the same area of G2 have an intermediate composition between biotic and abiotic end-members.

4.3. *Equilibrium temperature of hydrothermal gases*

The elemental composition of the gases of Petite Terre shows a general low concentration of H_2 and CO in both BAS and Dziani Dzaha Lake areas. Therefore, although H_2 and CO are considered useful geoindicators for equilibrium temperature and pressure in the hydrothermal system, we did not consider these species to be suitable for thermobarometric purposes in the study of Mayotte fluids. On the contrary, the amounts of CO_2 and methane (Tables 1a–1e) are high enough to have good analytical precision in both concentration and isotopic data. Therefore, we used the approach adopted by Liuzzo et al. [2021], assuming that in the hydrothermal system an equilibrium is attained between the dominant species H_2O–H_2–CO_2–CO–CH_4, in which the formation of methane is favoured by the decreasing temperature from the reaction (A4) indicated in Appendix A.4. For this system, the temperature has been calculated assuming a condition of thermal equilibrium between CH_4 and CO_2 by (A5) in Appendix A.4 as proposed by Giggenbach [1992]. Moreover, in order to further constrain the possible evidence of recent input of deep fluids in the Mayotte hydrothermal system, we evaluated the thermal equilibrium in combination with their isotopic signatures based on their $\delta^{13}C$ isotopic fractionation factor between CO_2 and CH_4. To this aim, we combined the temperatures obtained from (A5) with the temperatures calculated using (A6) proposed by Bottinga [1969], valid for temperatures ranging between 0–700 °C (Appendix A.4), following the approach proposed in Ono et al. [1993], and recently applied in the Comoros area by Liuzzo et al. [2021], finally obtaining (A7). On this basis, the curves of thermal equilibrium were modeled assuming that both chemical and isotopic equilibrium is maintained with a fixed $\delta^{13}C_{C02}$ representative of the possible range of magmatic signature; here we considered a range of $\delta^{13}C_{C02}$ magmatic signatures from $-4‰$ to $-8‰$ when coupling (A5) and (A6).

The results are shown in Figure 9, which allows to extend the preliminary study made by Liuzzo et al. [2021], taking into account recent gas sampling in 2020 at both BAS and Dziani Dzaha Lake areas of Petite Terre. The data considered are those in which there are no obvious secondary variations and/or

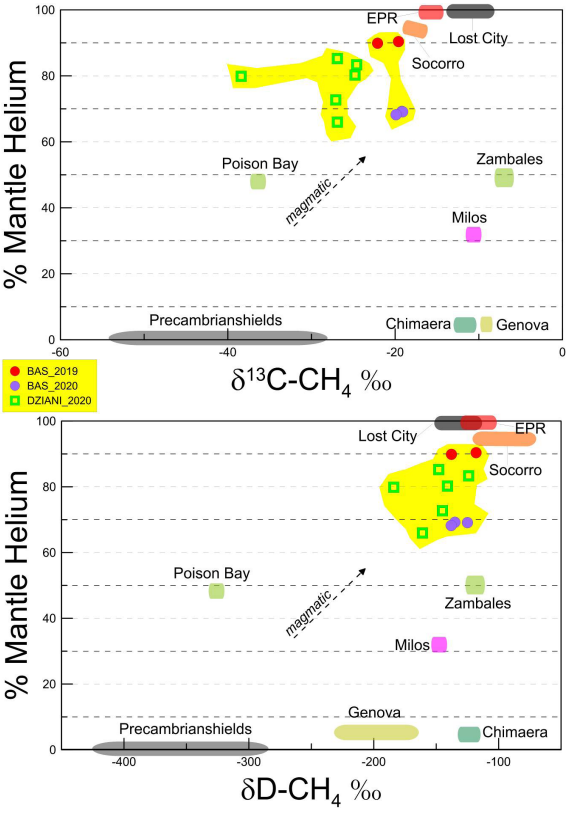

Figure 8. $\delta^{13}C$ and δD in CH_4 versus the proportion of He sourced from the mantle (%He). The Petite Terre data are compared with a larger dataset from various geodynamic origins from Etiope and Sherwood Lollar [2013], and appear consistent with environments where methane of magmatic origin is clearly recognized.

gas–water interactions.

The methane-rich gases at the Dziani Dzaha Lake are certainly conditioned by the microbial activity in lacustrine waters and sediments; the range of variability of $\delta^{13}C_{(CH_4)}$ and δD is high, and the values are generally scattered. The variability of $\delta^{13}C_{(CO_2)}$ is less than for $\delta^{13}C_{(CH_4)}$; however, $\delta^{13}C_{(CO_2)}$ of gases bubbling through the Dziani Dzaha Lake show a wider range of variability than BAS. As noted in the previous sections, this leads us to conclude that outgassing in Dziani Dzaha Lake is probably affected by several physicochemical processes and are related to several sources. Their isotopic variability is related to variable degrees of mixing between organic and abiotic components [Milesi et al., 2020]. Figure 9 also shows that isotopic equilibrium is not reached between CO_2 and CH_4, as all sampled gases at Dziani Dzaha Lake have variable $\delta^{13}C_{(CH_4)}$ values above the calculated equilibrium curves. Bacterial oxidation of CH_4 likely controls isotopic fractionation, determining an increase in the isotopic ratio in the residual methane [Baker and Fritz, 1981, Coleman et al., 1981, Horita, 2001], and this process is expected to be significant in the Dziani Dzaha Lake, where an extensive microbial activity has been well documented.

Regarding the BAS area, the range of variability of $\delta^{13}C_{(CH_4)}$ is consistent with an abiogenic source [Schoell, 1980], and the data also show moderate variability in their isotopic signature. Therefore, a single degassing source produces the bubbling observed at BAS. In the 2020 samples, however, a significant shift of the methane toward heavier isotopic concentrations, as observed in Liuzzo et al. [2021] is still evident. Although a carbon isotopic fractionation of methane cannot be excluded in BAS area as in Dziani, Liuzzo et al. [2021] have shown that isotopic signature of the hydrothermal gases in the BAS area likely records a quenching effect. In this interpretation, CO_2 and CH_4 are considered initially in isotopic equilibrium during outgassing of the deep (mantle level) magmatic source. In this interpretation, isotopic disequilibrium is a consequence of fast ascent of the gases to shallow crustal layers, with little time for isotopic re-equilibration. Such a quenching effect is expected because of the much faster rate of re-equilibration (about 100 times) of the elemental reaction with respect to the isotopic one [Giggenbach, 1982]. Our new dataset confirms that isotopic disequilibrium between CO_2 and CH_4 previously shown in 2018–2019 samples, is still well recorded by the 2020 samples. An important consequence of the disequilibrium is that the actual temperatures could be higher than those calculated from the equilibrium obtained from (A5), as discussed by Liuzzo et al. [2021]. This is because, having numerically simulated a thermal isotopic-chemical equilibrium between CO_2, CH_4 and their d $\delta^{13}C$, the corresponding $\delta^{13}C$ values of methane would be in equilibrium if they intersected the corresponding curve. However, the $\delta^{13}C(CH_4)$ values would have to shift to the left to meet the equilibrium curve and thus would have even higher temperatures.

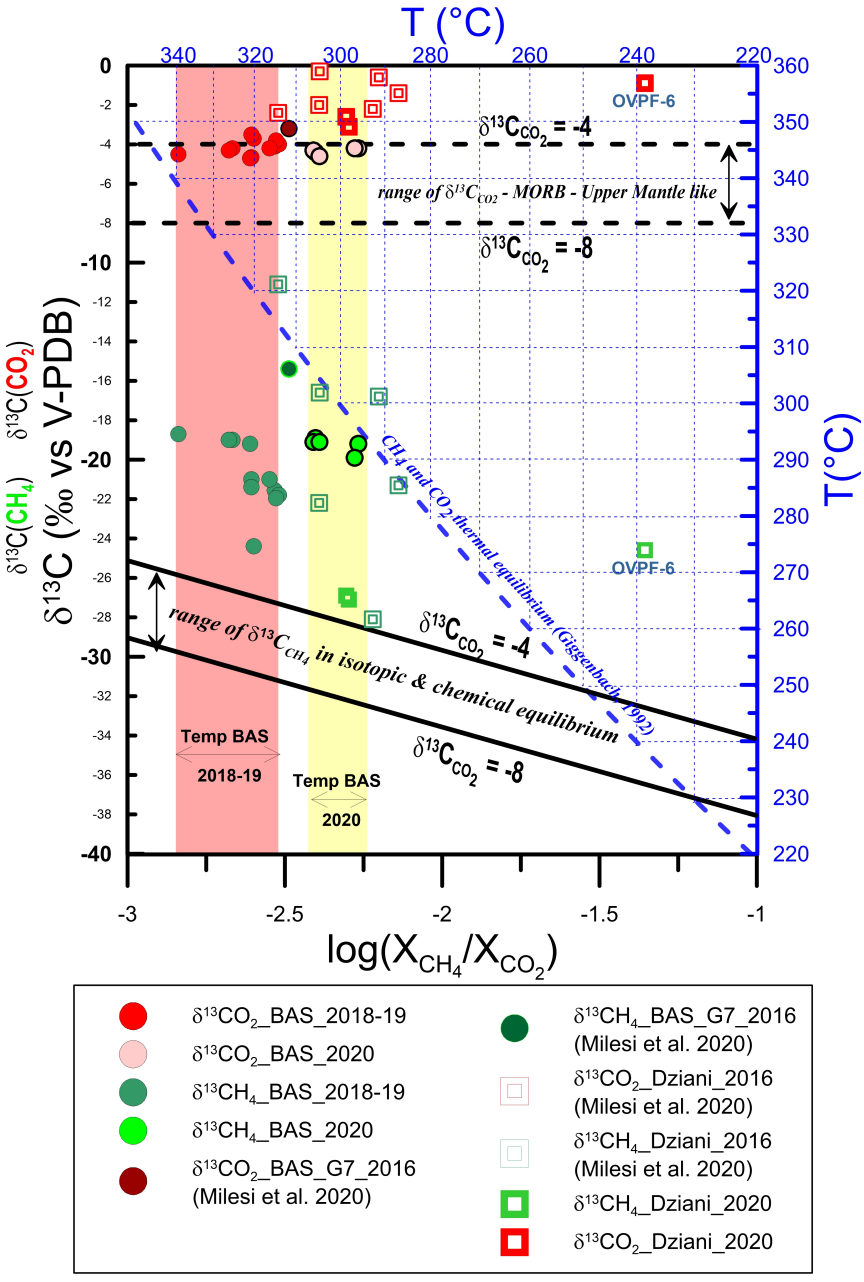

Figure 9. $\delta^{13}C$ in CO_2 (red) and CH_4 (green) versus $\log(X_{CH_4}/X_{CO_2})$ for Petite Terre bubbling gases. Red and yellow areas correspond to the range of equilibrium temperature of the hydrothermal gas samples collected in the BAS area between 2018 and 2020, respectively. The blue dashed line corresponds to the CH_4 and CO_2 thermal equilibrium expressed in (A5) in Appendix A.4 [Giggenbach, 1992]; the continuous black lines are calculated following (A7) in Appendix A.4 by assuming isotopic and chemical equilibrium between CH_4 and CO_2 for two possible end-members of $\delta^{13}C$ (CO_2) at −4‰ and −8‰, which in turn are indicated as horizontal black dashed lines.

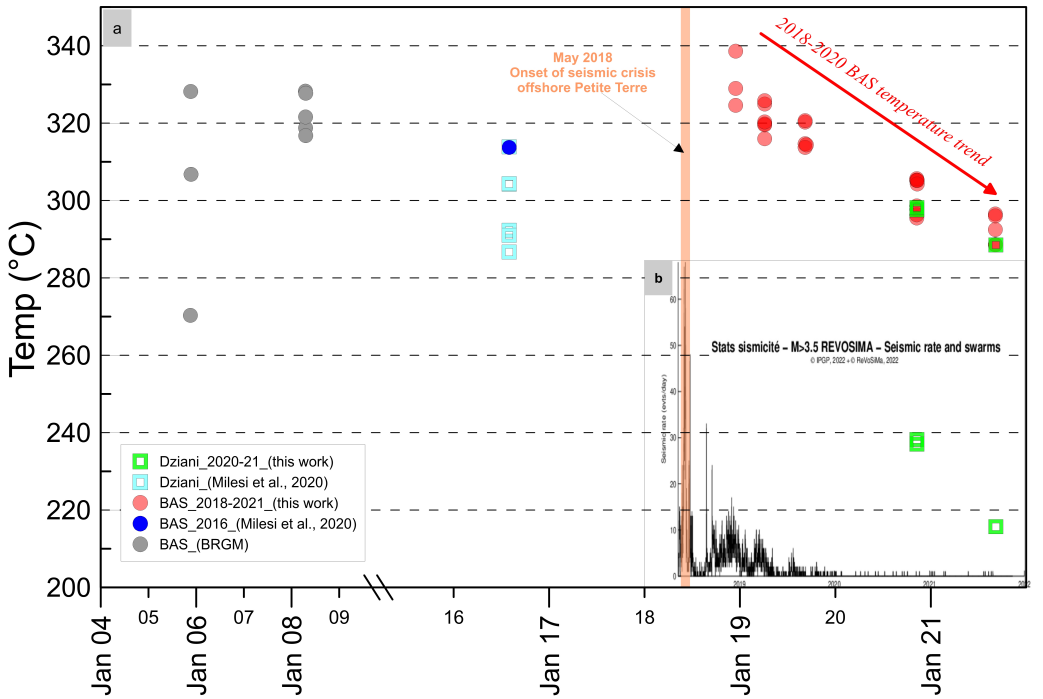

Figure 10. (a) Time evolution of equilibrium temperature in hydrothermal fluids of Mayotte (Petite Terre) calculated by using (A4) from Giggenbach, 1992 (Appendix A.4). In box (b), overlaid in time, the declining rate of seismicity (event/day for M > 3.5 earthquakes; from REVOSIMA Monthly Bulletin—December 2021) since the beginning of the volcano-tectonic crisis in 2018.

The occurrence of isotopic disequilibrium implies that the hydrothermal system at BAS may have recently received new input of deep-hot CO_2 and CH_4-rich gases possibly before or at the beginning of the volcanic activity in 2018.

This hypothesis is further supported by the time evolution of the equilibrium temperatures (calculated with (A5)) over years in both the BAS and Dziani areas (Figure 10). In the BAS area, a well-defined trend of cooling can be observed between 2018 and 2021. The equilibrium temperature of gases collected in the Dziani Dzaha Lake follows the same trend even if the dataset is smaller and the gases have been variably affected by secondary processes. The cooling trend recorded by equilibrium temperatures mimics that of progressive decrease of the seismic activity and magma extrusion rate over the same time period [Bachèlery et al., 2019, Berthod et al., 2021a,b, Cesca et al., 2020, Feuillet et al., 2021, Lemoine et al., 2020, REVOSIMA, 2019; REVOSIMA Monthly Bulletin, December 2021]. It is therefore reasonable to assume that a deep fluid input, which was somehow related to the most intense phase of submarine eruptive activity, may have reached the outgassing areas of Petite Terre, resulting in the initial increase in equilibrium temperature and isotopic disequilibrium in the hydrothermal system, which then over time fell steadily, as the seismo-volcanic crisis declined. The existence of this link is expected as most of the seismicity and the deep sources of magma feeding the distal submarine eruption are located close to Petite Terre (5–15 km) [Foix et al., 2021] and the involved volumes of magma are huge and CO_2-rich [Feuillet et al., 2021, Berthod et al., 2021a,b].

5. Conclusion

This study has investigated the geochemistry of the two main areas of low-T gas seeps occurring at Mayotte (Petite Terre): the Airport tidal flat (BAS) and the

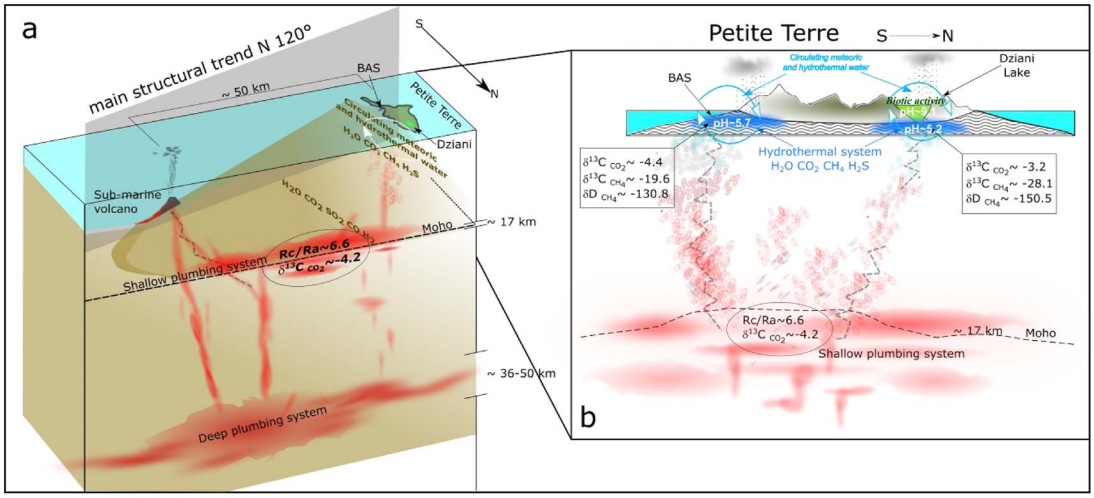

Figure 11. (a) Conceptual diagram of the deep and shallow magma and fluid plumbing system [modified from Berthod et al., 2021a,b] beneath the eastern flank of Mayotte Island. (b) Detail of the signatures and transfer of magmatic fluids reaching the two gas seep areas of Petite Terre (BAS and Dziani Dzaha Lake).

intracrateric Dziani Dzaha Lake. The chemical and isotopic study has permitted to constrain both the sources and the secondary processes controlling the signature of the bubbling hydrothermal fluids.

The CO_2-rich bubbling gases streaming through Petite Terre Island are sourced by the shallower part of the deep magmatic plumbing located near the Moho at about 17 km b.s.l. [Foix et al., 2021, Berthod et al., 2021a,b] (Figure 11a). This inference stems from the homogeneous and low He/Ar* ratios of Mayotte gases and the absence of crustal signature in their chemical and isotopic signatures. The seismically very active magmatic system is located close to the island (5–15 km) and has likely provided the CO_2–He rich fluids percolating through the whole deep magma plumbing system, whose deeper part is located in the mantle (around 36–50 km depth), has a basanitic composition and is expected to be very CO_2 rich [Berthod et al., 2021a,b]. Petrological and geophysical data show that both the deep (mantle) and the shallow (crustal underplating) parts of the plumbing systems were drained to feed the recent submarine eruptive activity responsible for the construction of the huge volcanic edifice about 50 km offshore Petite Terre [Berthod et al., 2021a, Cesca et al., 2020, Feuillet et al., 2019, Lemoine et al., 2020]. Seismic and eruptive activity have steadily declined since the beginning of the crisis in 2018. This evolution is likely recorded by the decrease over time of equilibrium temperatures in Petite Terre hydrothermal fluids.

Hydrothermal gases bubbling in both the BAS and Dziani Dzaha Lake reflect primarily the signature of deep gases in terms of geochemical tracers such as R/R_a δ^{13}C in carbon and methane (Figure 11b), however their chemical and isotopic composition is partly affected by secondary processes that produce some variability between the two areas. The Dziani Dzaha Lake hosts the only CH_4-dominated bubbling area and gases streaming through the lake are variable and in some cases significantly affected by microbial activity in a meromictic lake environment. In the BAS tidal area, the influence of the microbial activity and of the gas–water interaction is certainly less significant. Secondary processes in the Dziani Dzaha Lake explain the significant difference in the methane isotopic signature. Conversely, the He content and isotopic signature is much less affected by late-stage processes and preserved the signature of the pristine deep source.

The recognition in the BAS area of deep gases related to the several stages of outgassing from the magmatic plumbing system and not affected by secondary processes, make this area the most suitable area for volcano monitoring purposes.

Conflicts of interest

Authors have no conflict of interest to declare.

Acknowledgements

This work is part of the PhD (XXXIV cycle) of Marco Liuzzo at the University of Ferrara. The work has been partially funded by INGV (GECO project Fondi Ricerca libera 2019 INGV) and by REVOSIMA Consortium (IPGP, CNRS, BRGM, IFREMER) for fieldwork and and by the Interreg "Hatari" (IPGP/OVPF) for analytical activities. The authors are very thankful to INGV, Sezione di Palermo, for allowing the access to the analytical facilities and to the BRGM Mayotte for their support during fieldwork.

Appendix A.

A.1. R_c/R_a *calculation*

The $^3He/^4He$ ratio is expressed as R/R_a (being R_a the He isotope ratio of air and equal to 1.39×10^{-6}) with an analytical uncertainty (1σ) below 0.3%. The $^3He/^4He$ ratio corrected for atmospheric contamination has been calculated using the measured $^4He/^{20}Ne$ ratio following Sano and Wakita [1985] and is reported in units of R_c/R_a, as follows:

$$\frac{R_c}{R_a} = \frac{\left(\frac{R_m}{R_a}\right)\cdot\left(\frac{^4He}{^{20}Ne}\right)_m - \left(\frac{^4He}{^{20}Ne}\right)_a}{\left(\frac{^4He}{^{20}Ne}\right)_m - \left(\frac{^4He}{^{20}Ne}\right)_a} \quad \text{(A1)}$$

where subscripts m and a refer to measured and atmosphere theoretical values respectively [$(He/Ne)_a = 0.318$ [Ozima and Podosek, 1983]]. As a consequence of a very low air contamination the correction on the $^3He/^4He$ ratio is small or negligible for most of the gas samples ($^4He/^{20}Ne)_m \gg (^4He/^{20}Ne)_a$.

A.2. *Argon correction*

^{40}Ar was corrected for air contamination ($^{40}Ar^*$) in samples showing $^{40}Ar/^{36}Ar > 315$ assuming that the ^{36}Ar present derived from atmosphere, as follows:

$$^{40}Ar^* = {}^{40}Ar_{sample} - {}^{36}Ar_{sample}\cdot\left(\frac{^{40}Ar}{^{36}Ar}\right)_{air}. \quad \text{(A2)}$$

A.3. $\delta^{13}C_{CO_2}$ *calculation in a Rayleigh fractionation under dissolution equilibrium*

In order to constrain the pristine C isotopic signature of CO_2 in Mayotte, we modeled a Rayleigh fractionation assuming dissolution under equilibrium conditions based on the approach used in Rizzo et al. [2019] and Liuzzo et al. [2021] for the application in the previous study for Comoros archipelago. The Clark and Fritz [1997] equation is as follows:

$$\delta^{13}C_{CO_2} = (\delta^{13}C_{CO_2})_0 + \varepsilon\ln(f) \quad \text{(A3)}$$

where the subscript 0 indicates the initial CO_2 isotope composition and f is the fraction of the residual gas phase, while ε is the fractionation factor between DIC (dissolved inorganic carbon) and gaseous CO_2 ($CO_{2\cdot(g)}$). In turn, ε depends on water temperature and pH, which are unknown. In the discussion, the values of temperature and pH 5.7 and T = 32 °C (curve Rf-1; Figure 5a) correspond to those measured in the marine water of the Mayotte tidal flat by BRGM surveys [Sanjuan et al., 2008, Traineau et al., 2006]. The curve Rf-2 has been calculated using a pH = 9 and T = 36 °C, that correspond to the parameters measured in Dziani by Milesi et al. [2020]. Further fractionation lines were calculated either for lower pH (Rf-3 trend; pH = 5.2 and T = 36 °C) or higher temperature (Rf-4 trend; pH = 9 and T = 102 °C).

A.4. *Equilibrium temperature*

Assuming that in the hydrothermal system an equilibrium is attained between the dominant species H_2O–H_2–CO_2–CO–CH_4, methane can form inorganically from the Sabatier reaction [Hulston and McCabe, 1962]:

$$CO_2 + 4H_2 = CH_4 + 2H_2O \quad \text{(A4)}$$

where the formation of methane is favoured by the decreasing temperature. For this system, we calculated the condition of thermal equilibrium between CH_4 and CO_2 following the equation proposed by Giggenbach [1992]:

$$\log(X_{CH_4}/X_{CO_2}) = 4625/(t_e + 273) - 10.4. \quad \text{(A5)}$$

The equilibrium temperature for the isotopic fractionation of $\delta^{13}C$ between CO_2 and CH_4 was calculated using the equation proposed by Bottinga [1969] valid for temperatures ranging between 0–700 °C:

$$\Delta = 22166/(t_e + 273) - 13.8 \quad \text{(A6)}$$

where Δ is the difference between $\delta^{13}C_{CO_2}$ and $\delta^{13}C_{CH_4}$ values.

In Figure 7 the thick black lines were modeled assuming that both chemical and isotopic equilibrium is maintained with a fixed $\delta^{13}C_{C02}$ corresponding to the range of magmatic signature ($-4‰$ and $-8‰$; dashed black lines) by coupling the Equations (A5) and (A6):

$$\log\left(\frac{X_{CH_4}}{X_{CO_2}}\right) = \frac{4625(\Delta + 13.8)}{22166} - 10.4. \qquad \text{(A7)}$$

References

Aiken, C., Saurel, J. M., and Foix, O. (2021). Earthquake location and detection modeling for a future seafloor observatory along Mayotte's volcanic ridge. *J. Volcanol. Geotherm. Res.*, 418, article no. 107322.

Bachèlery, P., Berthod, C., Di Muro, A., Gurioli, L., Besson, P., Caron, B., Jorry, S., Fouquet, Y., Nowak, S., Burckel, P., Devidal, J. L., Deplus, C., Thinon, I., Bickert, M., Boudon, G., Moreira, M. A., Chauvel, C., Le Friant, A., and Feuillet, N. (2019). Petrological and geochemical characterization of the lava from the 2018–2019 mayotte eruption: first results. In *AGU Fall Meeting Abstracts*, pages V52D–06. AGU, Washington, DC.

Bachèlery, P. and Hémond, C. (2016). Geochemical and petrological aspects of karthala volcano. In Bachèlery, P., Lénat, J.-F., Di Muro, A., and Michon, L., editors, *Active Volcanoes of the Southwest Indian Ocean: Piton de La Fournaise and Karthala*, pages 367–384. Springer-Verlag, Berlin, Heidelberg.

Baker, J. F. and Fritz, P. (1981). Carbon isotope fractionation during microbial methane oxidation. *Nature*, 293, 289–291.

Barry, P. H. and Hilton, D. R. (2016). Release of subducted sedimentary nitrogen throughout Earth's mantle. *Geochem. Perspect. Lett.*, 2, 148–159.

Barry, P. H., Hilton, D. R., Füri, E., Halldórsson, S. A., and Grönvold, K. (2014). Carbon isotope and abundance systematics of Icelandic geothermal gases, fluids and subglacial basalts with implications for mantle plume-related CO_2 fluxes. *Geochim. Cosmochim. Acta*, 134, 74–99.

Batista Cruz, R. Y., Rizzo, A. L., Grassa, F., Bernard Romero, R., González Fernández, A., Kretzschmar, T. G., and Gómez-Arias, E. (2019). Mantle degassing through continental crust triggered by active faults: The case of the Baja California Peninsula, Mexico. *Geochem. Geophys. Geosyst.*, 20(4), 1912–1936.

Berthod, C., Médard, E., Bachèlery, P., Gurioli, L., Di Muro, A., Peltier, A., Komorowski, J., Benbakkar, M., Devidal, J., Langlade, J., Besson, P., Boudon, G., Rose-Koga, E., Deplus, C., Le Friant, A., Bickert, M., Nowak, S., Thinon, I., Burckel, P., Hidalgo, S., Jorry, S., Fouquet, Y., and Feuillet, N. (2021a). The 2018-ongoing Mayotte submarine eruption: magma migration imaged by petrological monitoring. *Earth Planet Sci. Lett.*, 571, article no. 117085.

Berthod, C., Médard, E., Di Muro, A., Hassen Ali, T., Gurioli, L., Chauvel, C., Komorowski, J.-C., Bachèlery, P., Peltier, A., Benbakkar, M., Devidal, J.-L., Besson, P., Le Friant, A., Deplus, C., Nowak, S., Thinon, I., Burckel, P., Hidalgo, S., Feuillet, N., Jorry, S., and Fouquet, Y. (2021b). Mantle xenolith-bearing phonolites and basanites feed the active volcanic ridge of Mayotte (Comoros archipelago, SW Indian Ocean). *Contrib. Mineral. Petrol.*, 176, article no. 75.

Bottinga, Y. (1969). Calculated fractionation factors for carbon and hydrogen isotope exchange in the system calcite-carbon dioxide-graphite-methane hydrogen-water vapor. *Geochim. Cosmochim. Acta*, 33, 49–64.

Boudoire, G., Rizzo, A. L., Arienzo, I., and Di Muro, A. (2020). Paroxysmal eruptions tracked by variations of helium isotopes: inferences from Piton de la Fournaise (La Réunion island). *Sci. Rep.*, 10, article no. 9809.

Boudoire, G., Rizzo, A. L., Di Muro, A., Grassa, F., and Liuzzo, M. (2018). Extensive CO_2 degassing in the upper mantle beneath oceanic basaltic volcanoes: First insights from Piton de la Fournaise volcano (La Réunion Island). *Geochim. Cosmochim. Acta*, 235, 376–401.

Bräuer, K., Kämpf, H., Koch, U., and Strauch, G. (2011). Monthly monitoring of gas and isotope compositions in the free gas phase at degassing locations close to the Nový Kostel focal zone in the western Eger Rift Czech Republic. *Chem. Geol.*, 290, 163–176.

Burnard, P. (2001). Correction for volatile fractionation in ascending magmas: noble gas abundances in primary mantle melts. *Geochim. Cosmochim. Acta*, 65(15), 2605–2614.

Cadeau, P., Jézéquel, D., Leboulanger, C., Fouilland, E., Le Floc'h, E., Chaduteau, C., Milesi, V., Guélard, J., Sarazin, G., Katz, A., d'Amore, S., Bernard, C., and Ader, M. (2020). Carbon isotope evidence for large methane emissions to the Proterozoic atmosphere. *Sci. Rep.*, 10, article no. 18186.

Capasso, G., Carapezza, M. L., Federico, C., Inguaggiato, S., and Rizzo, A. (2005). Geochemical variations in fluids from Stromboli volcano (Italy): early evidences of magma ascent during 2002-2003 eruption. *Bull. Volcanol.*, 68, 118–134.

Cesca, S., Letort, J., Razafindrakoto, H. N., Heimann, S., Rivalta, E., Isken, M. P., Nikkhoo, M., Passarelli, L., Petersen, G. M., Cotton, F., and Dahm, T. (2020). Drainage of a deep magma reservoir near Mayotte inferred from seismicity and deformation. *Nat. Geosci.*, 13(1), 87–93.

Clark, I. D. and Fritz, P. (1997). *Environmental Isotopes in Hydrogeology*. CRC Press, Boca Raton, FL.

Class, C., Goldstein, S. L., Stute, M., Kurz, M. D., and Schlosser, P. (2005). Grand Comore Island: a well-constrained "low ^{3}He/^{4}He". *Earth Planet. Sci. Lett.*, 233, 391–409.

Coffin, M. F., Rabinowitz, P. D., and Houtz, R. E. (1986). Crustal structure in the western Somali Basin. *Geophys. J. Int.*, 86(2), 331–369.

Coleman, D. D., Risatti, J. B., and Schoell, M. (1981). Fractionation of carbon and hydrocarbon isotopes by methane-oxidizing bacteria. *Geochim. Cosmochim. Acta*, 45, 1033–1037.

Etiope, G. and Sherwood Lollar, B. (2013). Abiotic methane on Earth. *Rev. Geophys.*, 51, 276–299.

Famin, V., Michon, L., and Bourhane, A. (2020). The Comoros archipelago: a right-lateral transform boundary between the Somalia and Lwandle plates. *Tectonophysics*, 789, article no. 228539.

Feuillet, N., Jorry, S., Crawford, W. C., Deplus, C., Thinon, I., Jacques, E., Saurel, J. M., Lemoine, A., Paquet, F., Daniel, R., Gaillot, A., Satriano, C., Peltier, A., Aiker, C., Foix, O., Kowalski, P., Laurent, A., Beauducel, F., Grandin, R., Ballu, V., Bernard, P., Donval, J. P., Géli, L., Gomez, J., Pelleau, P., Guyader, V., Rinnert, E., Besancon, S., Bertil, D., Lemarchand, A., and Vanderwoerd, J. (2019). Birth of a large volcano offshore Mayotte through lithosphere-scale rifting. In *Proceedings of the AGU Fall Meeting 2019*. AGU, Washington, DC.

Feuillet, N., Jorry, S., Crawford, W. C., Deplus, C., Thinon, I., Jacques, E., Saurel, J. M., Lemoine, A., Paquet, F., Satriano, C., Aiken, C., Foix, O., Kowalski, P., Laurent, A., Rinnert, E., Cathalot, C., Donval, J.-P., Guyader, V., Gaillot, A., Scalabrin, C., Moreira, M., Peltier, A., Beauducel, F., Grandin, R., Ballu, V., Daniel, R., Pelleau, P., Gomez, J., Besançon, S., Geli, L., Bernard, P., Bachelery, P., Fouquet, Y., Bertil, D., Lemarchand, A., and Van der Woerd, J. (2021). Birth of a large volcanic edifice offshore Mayotte via lithosphere-scale dyke intrusion. *Nat. Geosci.*, 14, 787–795.

Foix, O., Aiken, C., Saurel, J. M., Feuillet, N., Jorry, S. J., Rinnert, E., and Thinon, I. (2021). Offshore Mayotte volcanic plumbing revealed by local passive tomography. *J. Volcanol. Geotherm. Res.*, 420, article no. 107395.

Gaina, C., Torsvik, T. H., van Hinsbergen, D. J. J., Medvedev, S., Werner, S. C., and Labails, C. (2013). The African Plate: a history of oceanic crust accretion and subduction since the Jurassic. *Tectonophysics*, 604, 4–25.

Giggenbach, W. F. (1982). Carbon-13 exchange between CO_2 and CH_4 under geothermal conditions. *Geochim. Cosmochim. Acta*, 46, 159–165.

Giggenbach, W. F. (1992). Chemical techniques in geothermal exploration. Applications of geochemistry in geothermal reservoir development. In D'Amore, F., editor, *Activities at the UNITAR/UNDP Centre on Small Energy Resources for 1988*, pages 119–143. UNITAR/UNDP Centre on Small Energy Resources, Rome.

Giggenbach, W. F. and Goguel, R. L. (1989). Methods for the collection and analysis of geothermal and volcanic water and gas samples. New Zealand Department of Scientific and Industrial Research, Chemistry Division Report 2387, 53 p.

Gilfillan, S., Lollar, B., Holland, G., Blagburn, D., Stevens, S., Schoell, M., Cassidy, M., Ding, Z., Zhou, Z., Lacrampe-Couloume, G., and Ballentine, C. J. (2009). Solubility trapping in formation water as dominant CO_2 sink in natural gas fields. *Nature*, 458, 614–618.

Hoefs, J. (2015). *Stable Isotope Geochemistry*. Springer International Publishing, Switzerland, 7th edition. ISBN 978-3-319-19715-9.

Horita, J. (2001). Carbon isotope exchange in the system CO_2–CH_4 at elevated temperatures. *Geochim. Cosmochim. Acta*, 65(12), 1907–1919.

Hulston, J. R. and McCabe, W. J. (1962). Mass spectrometer measurements in the thermal areas of

New Zealand: Part 1. Carbon dioxide and residual gas analyses. *Geochim. Cosmochim. Acta*, 26(3), 383–397.

Lemoine, A., Briole, P., Bertil, D., Roullé, A., Foumelis, M., Thinon, I., Raucoules, D., de Michele, M., Valty, P., and Hoste Colomer, R. (2020). The 2018–2019 seismo-volcanic crisis east of Mayotte, Comoros islands: seismicity and ground deformation markers of an exceptional submarine eruption. *Geophys. J. Int.*, 23(1), 22–44.

Liuzzo, M., Di Muro, A., Rizzo, A. L., Caracausi, A., Grassa, F., Fournier, N., Shafik, B., Boudoire, G., Coltorti, M., Moreira, M., and Italiano, F. (2021). Gas geochemistry at Grande Comore and Mayotte volcanic islands (Comoros archipelago). *Indian Ocean Geochem. Geophys. Geosyst.*, 22, article no. e2021GC009870.

Marty, B. (2012). The origins and concentrations of water, carbon, nitrogen and noble gases on earth. *Earth Planet. Sci. Lett.*, 313–314, 56–66.

Mazzini, A., Svensen, H., Etiope, E., Onderdonk, N., and Banks, D. (2011). Fluid origin, gas fluxes and plumbing system in the sediment-hosted Salton Sea Geothermal System (California, USA). *J. Volcanol. Geotherm. Res.*, 205, 67–83.

Michon, L. (2016). The volcanism of the Comoros archipelago integrated at a regional scale. In Bachèlery, P., Lénat, J.-F., Di Muro, A., and Michon, L., editors, *Active Volcanoes of the Southwest Indian Ocean:Piton de La Fournaise and Karthala*, pages 333–344. Springer-Verlag, Berlin and Heidelberg.

Milesi, V. P., Debure, M., Marty, N. C. M., Capano, M., Jézéquel, D., Steefel, C., Rouchon, V., Albéric, P., Bard, E., Sarazin, G., Guyot, F., Virgone, A., Gaucher, E. C., and Ader, M. (2020). Early diagenesis of lacustrine carbonates in volcanic settings: the role of magmatic CO_2 (Lake Dziani Dzaha, Mayotte, Indian Ocean). *ACS Earth Space Chem.*, 4(3), 363–378.

Milesi, V. P., Jézéquel, D., Debure, M., Cadeau, P., Guyot, F., Sarazin, G., Claret, F., Vennin, E., Chaduteau, C., Virgone, A., Gaucher, E. C., and Ader, M. (2019). Formation of magnesium-smectite during lacustrine carbonates early diagenesis: Study case of the volcanic crater lake Dziani Dzaha (Mayotte Indian Ocean). *Sedimentology*, 66, 983–1001.

Nehlig, P., Lacquement, F., Bernard, J., Audru, J., Caroff, M., Deparis, J., Jaouen, T., Aziliz Pelleter, A., Perrin, J., Prognon, C., and Vittecoq, B. (2013). *Notice explicative de la carte géologique Mayotte à 1/30.000 feuille Mayotte*, volume 1179. BRGM, Orléans. Carte géologique par Lacquement F., Nehlig P., Bernard J. (2013).

Ono, A., Sano, Y., Wakita, H., and Giggenbach, W. F. (1993). Carbon isotopes of methane and carbon dioxide in hydrothermal gases of Japan. *Geochem. J.*, 27(4–5), 287–295.

Ozima, M. and Podosek, F. A. (1983). *Noble Gas Geochemistry*. Cambridge University Press, New York, NY.

Paonita, A., Caracausi, A., Iacono-Marziano, G., Martelli, M., and Rizzo, A. (2012). Geochemical evidence for mixing between fluids exsolved at different depths in the magmatic system of Mt Etna (Italy). *Geochim. Cosmochim. Acta*, 84, 380–394.

Phethean, J. J. J. (2016). Madagascar's escape from Africa: a high-resolution plate reconstruction for the Western Somali Basin and implications for supercontinent dispersal. *Geochem. Geophys. Geosyst.*, 17, 5036–5055.

Proskurowski, G., Lilley, M. D., Seewald, J. S., Früh-Green, G. L., Olson, E. J., Lupton, J. E., Sylva, S. P., and Kelley, D. S. (2008). Abiogenic hydrocarbon production at Lost City hydrothermal field. *Science*, 319, 604–607.

Quidelleur, X., Michon, L., Famin, V., Geffray, M. C., Danišík, M., Gardiner, N., Rusquet, A., and Zakaria, M. G. (2022). Holocene volcanic activity in Anjouan Island (Comoros archipelago) revealed by new Cassignol–Gillot groundmass K–Ar and 14C ages. *Quat. Geochronol.*, 67, article no. 101236.

REVOSIMA (2019). Bulletin n°1 de l'activité sismo-volcanique à Mayotte, IPGP. Université de Paris, OVPF, BRGM, Ifremer, CNRS, 23 August 2019, http://www.ipgp.fr/sites/default/files/ipgp_1er_bulletin_info_sismo_volcanique_mayotte-cor.pdf and http://www.ipgp.fr/revosima.

REVOSIMA (2021). Bulletin n°1 de l'activité sismo-volcanique à Mayotte. IPGP, Université de Paris, OVPF, BRGM, Ifremer, CNRS, 31 December 2021, http://www.ipgp.fr/sites/default/files/ipgp_revosima_n37_20220106.pdf and http://www.ipgp.fr/revosima.

Rizzo, A. L., Caracausi, A., Chavagnac, V., Nomikou, P., Polymenakou, P. N., Mandalakis, M., Kotoulas, G., Magoulas, A., Castillo, A., Lampridou, D., Marusczak, N., and Sonke, J. E. (2019). Geochemistry of CO_2-Rich Gases Venting From Submarine Volcan-

ism: The Case of Kolumbo (Hellenic Volcanic Arc, Greece). *Front. Earth Sci.*, 7, article no. 60.

Sanjuan, B., Baltassat, J.-M., Bezelgues, S., Brach, M., Girard, J.-F., and Mathieu, F. (2008). Estimation du potentiel géothermique de Mayotte: Phase 2 - Etape 2. Investigations géologiques, géochimiques et géophysiques complémentaires, synthèse des résultats. BRGM/RP-568082 Final reports, 82 p., 18 Figure, 3 Tables, 6 ann. BRGM, Orléans.

Sano, Y. and Marty, B. (1995). Origin of carbon in fumarolic gases from island arcs. *Chem. Geol.*, 119, 265–274.

Sano, Y. and Wakita, H. (1985). Geographical distribution of ^{3}He/^{4}He ratios in Japan: implications for arc tectonics and incipient magmatism. *J. Geophys. Res.*, 90, 8729–8741.

Schoell, M. (1980). The hydrogen and carbon isotopic composition of methane from natural gases of various origins. *Geochim. Cosmochim. Acta*, 44, 649–661.

Stamps, D. S., Kreemer, C., Fernandes, R., Rajaonarison, T. A., and Rambolamanana, G. (2021). Redefining east African rift system kinematics. *Geology*, 49(2), 150–155.

Taran, J. A., Varley, N. R., Inguaggiato, S., and Cienfuegos, E. (2010b). Geochemistry of H_{2-} and CH_4-enriched hydrothermal fluids of Socorro Island, Revillagigedo Archipelago, Mexico. Evidence for serpentinization and abiogenic methane. *Geofluids*, 10, 542–555.

Taran, Y. A., Kliger, G. A., Cienfuegos, E., and Shuykin, A. N. (2010a). Carbon and hydrogen isotopic compositions of products of open-system catalytic hydrogenation of CO_2: implications for abiogenic hydrocarbons in Earth's crust. *Geochim. Cosmochim. Acta*, 74, 6112–6125.

Thivet, S., Carlier, J., Gurioli, L., Di Muro, A., Besson, P., Smietana, M., Boudon, G., Bachèlery, P., Eychenne, J., and Nedelec, J.-M. (2022). Magmatic and phreatomagmatic contributions on the ash-dominated basaltic eruptions: insights from the April and November–December 2005 paroxysmal events at Karthala volcano, Comoros. *J. Volcanol. Geotherm. Res.*, 424, article no. 107500.

Traineau, H., Sanjuan, B., Brach, M., and Audru, J.-C. (2006). Etat des connaissances du potentiel géothermique de Mayotte. Rapport final. BRGM/RP-54700-FR.

Tzevahirtzian, A., Zaragosi, S., Bachèlery, P., Biscara, L., and Marchès, E. (2021). Submarine morphology of the Comoros volcanic archipelago. *Mar. Geol.*, 432, article no. 106383.

Welhan, J. A. (1988). Origins of methane in hydrothermal systems. *Chem. Geol.*, 71, 183–198.

Welhan, J. A. and Craig, H. (1983). Methane, hydrogen and helium in hydrothermal fluids of 21″ N on the East Pacific Rise. In Rona, P. A., Bostriim, K., Laubier, L., and Smith Jr., K. L., editors, *Hydrothermal Processes at Seafloor Spreading Centers*, pages 391–409. Plenum, New York, NY.

Zinke, J., Reijmer, J. J. G., and Thomassin, B. A. (2001). Seismic architecture and sediment distribution within the Holocene barrier reef–lagoon complex of Mayotte (Comoro archipelago, SW Indian Ocean). *Palaeogeogr. Palaeoclimatol. Palaeoecol.*, 175(1–4), 343–368.